ELSEVIER

Progress in Quantum Electronics 37 (2013) 1–50

Progress in Quantum Electronics

www.elsevier.com/locate/pquantelec

Review

Recent developments in optofluidic-assisted Raman spectroscopy

Jacky S.W. Mak[a], Steve A. Rutledge[a], Rashid M. Abu-Ghazalah[a], Fatemeh Eftekhari[a], Juan Irizar[a], Natalie C.M. Tam[b], Gang Zheng[b], Amr S. Helmy[a,*]

[a]*The Edward S. Rogers Sr. Department of Electrical and Computer Engineering, University of Toronto, 10 King's College Road, Toronto, Ontario, Canada M5S 3G4*

[b]*Department of Medical Biophysics, University of Toronto, Canada*

Available online 12 December 2012

Abstract

This paper reviews and compares the different optofluidic techniques for enhancing the retrieved Raman signal in liquids with a focus on aqueous solutions. Recent progress in characterizing different nanostructures and biological molecules utilizing optofluidic fibers such as photonic crystal fibers (PCFs) in Raman spectroscopy are discussed. Techniques and applications to combine surface enhanced Raman spectroscopy (SERS) with optofluidic-assisted Raman spectroscopy are further reviewed. Finally, challenges and future opportunities to advance Raman spectroscopy combined with optofluidics are presented.

Keywords: Raman spectroscopy; Surface enhanced Raman spectroscopy; Capillary tubes; Photonic crystal fibers; Nanostructures; DNA

Contents

*Corresponding author. Tel.: +1 416 946 0199; fax: +1 416 971 3020.
E-mail address: a.helmy@utoronto.ca (A.S. Helmy).

0079-6727/$ - see front matter © 2012 Elsevier Ltd. All rights reserved.
http://dx.doi.org/10.1016/j.pquantelec.2012.11.001

1. Introduction

Raman spectroscopy has witnessed significant advances in its applicability since the discovery of the Raman effect by Sir C. V. Raman in 1928, and has established itself as a valuable analytical technique in a large number of different fields. It is currently being applied but not limited to the fields of art and archeology [1–5], pharmaceuticals [6–8], chemistry [9–12], biology [8,12–14], diagnostics [14–16], material science [17], forensics [18–20], and environmental monitoring [21–23]. Raman spectroscopy is known for its ability to rapidly and non-destructively provide information on the molecular vibrations of materials with exceptional specificity. Since molecular vibrations are specific to the molecular bonds and their symmetries, they are unique to every type of material at the molecular level. Therefore, spectra obtained from Raman spectroscopy, namely the Raman scattering, can also be described as the 'fingerprint' of materials. The collection of Raman spectra can be used to identify materials, as well as their properties such as stress/strain, doping, and crystallinity. However, the Raman effect is also an extremely weak process in which only one in 10 million photons are Raman scattered [24]. This low probability of the Raman scattering effect is responsible for the low sensitivity of Raman spectroscopy. As a result, this technique suffers from the background superimposed on the Raman modes by other stronger optical phenomena such as fluorescence. In the past two decades, advances in optical technologies and instrumentation have greatly improved the sensitivity of Raman spectroscopy. Until this present day, the sensitivity of Raman spectroscopy remains to be one of the challenges that is being improved through research in both academia and industry.

Moreover, owing to the weak sensitivity of Raman spectroscopy, its applications have been, and still are, largely limited to solid samples. In the liquid and gas state of materials, the density of the molecules is much lower than that in the solid state. In Raman spectroscopy, this means that there are fewer molecules to interact with the pump laser or excitation source to generate the Raman scattered signal. Thus, the Raman scattering effect is weaker in liquids, and it is even lower in weakly concentrated solutions and gases.

There are many variations of Raman spectroscopy developed with the aim of improving its sensitivity for samples in the liquid and gaseous state. For example, resonant Raman (RR) spectroscopy can be used to enhance the intensity of the Raman signal by tuning the pump laser frequency to match the excited electronic state of the molecules in question. This technique can enhance the Raman intensity by 2–6 orders of magnitude [25]. However, only a small number of Raman modes can be enhanced at any given time due to the frequency-matching condition. Moreover, a tunable laser with high power is usually required which is costly and often leads to photo-degradation of the sample.

Surface enhanced Raman spectroscopy (SERS) and tip-enhanced Raman spectroscopy (TERS) are two other techniques in which metallic nanostructures in close proximity, or adsorbed, to the analyte can improve the Raman signal through electromagnetic and chemical enhancement. In particular, SERS has demonstrated enhancement factors up to 9–10 orders of magnitude which enabled the detection of a single molecule [26–29]. However, metallic nanostructures are required to be mixed with the analyte to achieve this enhancement, which could alter the structure, chemical environment, or chemical properties of the analyte from its as-synthesized state due to conformational changes when interacting with metallic nanostructure. For example, hotspots created from metallic nanostructures could exert physical stress on the analyte, causing molecular reorientations [30]. Consequently, SERS often gives different Raman modes than normal Raman spectroscopy [31]. The positions and full width at half maximums (FWHMs) of the Raman modes, as well as the relative intensities between Raman modes could also be different between SERS spectra and normal Raman spectra. These differences further vary depending on the metallic structure used in the SERS measurement which makes analysis and interpretation of the spectra more difficult [32]. In addition, SERS only enhances some Raman modes of the analyte while suppressing the others depending on the orientation of the analyte relative to the metallic nanostructure [33,34]. Enhancements are also often not reproducible due to instability of the hotspots created [35]. In addition, the maximal enhancement factor could only be obtained through careful design of the metallic nanoparticles and tailored for a specific target analyte [36]. Furthermore, the metallic nanostructure might create additional background signal in the Raman spectrum, which would further complicate the analysis and interpretation of the Raman spectra [32].

For the aforementioned techniques, the efficiency in the process of generating and collecting Raman scatters in the practical scheme is not addressed, especially for liquid and gas samples. In conventional Raman spectroscopy, RR and SERS, the pump laser or excitation source is focused directly into the analyte to generate Raman scattering (Fig. 1). Most of the Raman signal retrieved at the detector is scattered from the beam waist of the pump laser at which the pump laser is most intense and the power density is the highest. In this case, the pump laser and the analytes are only interacting in the volume limited by the spot size of the pump laser in the lateral direction and the depth of field in the axial direction. Since Raman signals are scattered in omni-directions, only a fraction of the scattered signal is collected by the objective and detected by the detector due to the limited numerical aperture (NA) of the objective lens. In the case of a solution, the amount of Raman scattering detected from the small quantity of analyte dispersed in the buffer solution is minimal.

An alternative to increasing the sensitivity of Raman spectroscopy (not just for a few Raman modes of the analyte, but for all the Raman modes generated) while not altering the native state of the analyte is to incorporate optofluidic devices into the Raman

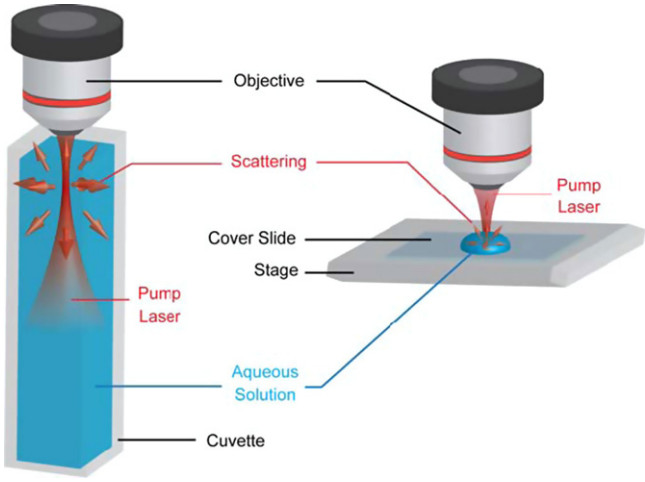

Fig. 1. Conventional Raman spectroscopy setup.

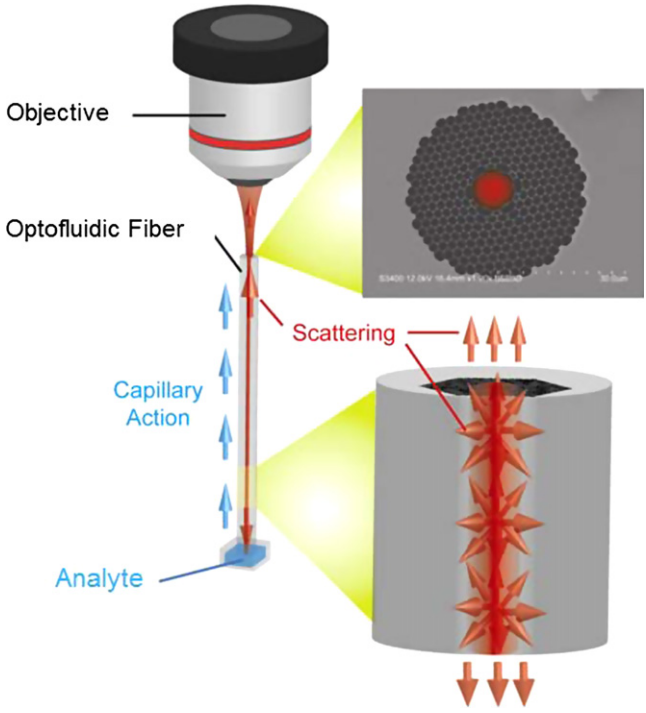

Fig. 2. Setup of Raman spectroscopy utilizing an optofluidic fiber as the medium for light–matter interactions.

spectroscopy setup as the interaction medium. Optofluidic devices enable the confinement of both the laser light and the liquid of interest into the same cavity, enabling a strong and efficient process of light–matter interaction. Fig. 2 shows an example of a Raman spectroscopy setup utilizing an optofluidic fiber as the light–matter interaction medium in

the backscattering configuration. In this example, the analyte is filled into the central core of the optofluidic fiber from the bottom end through capillary action. At the other end the pump laser light is focused into the same central core through the objective to generate Raman scattering signals from the analyte. Due to the strong confinement of the pump laser light in the optofluidic fiber, the pump laser light maintains a strong power density in the central core. As both the pump laser light and the analyte are confined within the same central core of the optofluidic fiber, the strongly confined pump laser can interact with the analyte throughout the entire fiber length. Thus, Raman signals are scattered throughout the entire length of the fiber as opposed to just the depth of field of the objective in the conventional scheme. Since Raman signals are mostly shifted by less than several tens of nanometers from the wavelength of the pump laser, they will also be confined inside the liquid core and collected throughout the fiber. As a result, the output signal from the fiber end will be collected more efficiently by the objective for detection; thus an enhanced Raman scattering signal could be retrieved at the detector.

An advantage to this technique is that prior knowledge of the analyte's electronic structure and surface chemistry is not required to enhance the retrieved Raman signal assuming that the pump laser light is within the guidance band of the optofluidic fiber after the liquid is injected. In RR and SERS, prior knowledge of the electronic structure and surface chemistry of the analyte is required to achieve Raman enhancement, respectively, which is not possible in applications where the exact composition of the sample is not known (e.g. forensic analysis).

In addition, most optofluidic fibers have core diameters on the order of a few microns. This means that only nano-liters to micro-liters of sample volumes are required for analysis. Furthermore, the advantage of long interaction length in optofluidic fibers can be extended through simply increasing the length of the optofluidic fiber. A longer interaction length can further enhance the retrieved Raman signal up to a certain length at which the enhancement factor will saturate due to large propagation losses. The relationship between the enhancement factor and the length of the optofluidic fiber will be discussed in detail in Section 2.5.

It is also important to note that the pump laser is confined inside the liquid core of the optofluidic fiber; thus, interactions between the pump laser light and the sidewall of the fiber are minimal. Therefore, the resulting interference due to the fiber material is limited in the presence of stronger Raman scattering signal from the analyte and any background. Furthermore, the use of optofluidic fiber does not increase the scattering cross-section, since optofluidic-assisted Raman spectroscopy enhances the 'retrieved Raman signal' (i.e. the Raman scattering signal retrieved at the detector). This is in contrast to techniques such as SERS or TERS where the Raman scattering cross-section is increased to achieve the enhancement in the Raman signal. Optofluidic devices described here are not limited to the fiber form. However, in this review, we will focus on optofluidic devices in the fiber form as the benefit of increased light–matter interaction could be obtained with fibers with centimeters in length. More importantly, further enhancement can be easily achieved with fiber length extended to meters without significant increases in complexity.

In this review, we will first describe and compare the different optofluidic devices used to enhance the retrieved Raman signal of liquid samples. Then, applications and recent progress in utilizing optofluidic-assisted Raman spectroscopy for characterizing nano-structures and biological molecules are reviewed. Finally, different techniques to combine SERS with optofluidic devices to achieve an ultimate sensitivity in Raman spectroscopy

are discussed, followed by a discussion of the outstanding challenges and opportunities for this platform.

2. Raman spectroscopy using different optofluidic devices

2.1. Capillary tubes

A capillary tube is the simplest form of optofluidic devices that provides a long path-length (i.e. centimeters to meters) for light–matter interaction. Capillary tubes are usually composed of a cladding made out of a solid material and a hollow core in which the liquid of interest is filled into for Raman analysis. When a liquid with a refractive index that is higher than that of the cladding is filled into the core of the capillary tube, the pump laser light can be guided through and interact with the liquid core of the capillary tube through total internal reflection (TIR). As the frequencies of the Raman scattered light generated in the liquid core are close to that of the pump laser light, this means they too can be guided in the liquid core onto the detector through TIR.

Traditionally, fused silica (or fused quartz) was used to form the cladding of most capillary tubes [37–39]. The first demonstration of enhancing the retrieved Raman signal with fused silica capillary tube was reported by Walrafen and Stone [37]. Raman signals of benzene and tetrachloroethylene were enhanced by a factor of 10^2–10^3 using a 20 m long fused silica capillary tube. However, as the refractive index of fused silica is ~1.46 at room temperature, this limits the liquids which can be tested because a refractive index of 1.46 is higher than most of the refractive indices of liquids common in life sciences such as aqueous solutions. As such, the application of fused silica capillary tube is limited to liquids that have high refractive indices [37–41].

Cladding materials that have indices of refraction lower than that of water ($n = 1.33$) were not available until Teflon-AF was manufactured by Dupont Corporation. Teflon-AF has a low refractive index of 1.29. Moreover, it is mechanically strong, thermally stable and transparent from the deep ultraviolet (UV) range to the near infrared (NIR) which make teflon capillary tubes (TCT) a suitable medium for light–matter interactions in Raman spectroscopy studies [42,43]. The use of TCT was demonstrated to enhance the retrieved Raman signals in various chemicals and biological analytes including aqueous carbonate solutions [43], isopropyl alcohol [44], creatinine in deionized water and urine [45], and β-carotene [46].

One main advantage of employing an optofluidic fiber is its enhancement of the light–matter interaction throughout the length of the fiber. Altkorn et al. compared the enhancement of the retrieved Raman signal using different lengths of TCT as well as different core and cladding dimensions [47]. By using methanol as a reference, a 532 nm excitation source, and a TCT with core diameter of 150 μm, a maximum enhancement factor of ~120 was achieved. This was a result of the improved coupling efficiency between the 150 μm core fiber and the objective used in the experiment through NA matching. The enhancement in the retrieved Raman signal with an extended TCT length in the backscattering geometry was also found to increase linearly for a short strand of TCT (i.e. < 1 m) and thereafter reached a plateau for a long TCT strand due to increased fiber losses. We will discuss and compare the performance of TCT with another type of optofluidic devices; namely photonic crystal fiber (PCF) for different fiber lengths in Section 2.5.

There are a few limitations to inherent with the use of TCTs for Raman spectroscopy. First, TCT emits photobleachable florescence that peaks at ~1500 cm^{-1} when excited by a 532 nm source, which may contribute to the background of the retrieved Raman spectrum [47]. Second, many molecules in their gas phase can permeate through Teflon-AF surfaces leading to leaks which would affect subsequent measurements [43]. The Teflon-AF surface is also hydrophobic, which makes it easier to trap air bubbles than glass capillary tubes and decrease its performance [43]. Although Teflon-AF has a lower refractive index than silica, it still has a higher refractive index than gases which limited its application to liquid analysis. The limited range of core diameters that is commercially available for TCT (i.e. greater than 50 μm) and the small refractive index contrast between Teflon-AF and most liquids also limit the guidance of the pump laser light in a highly multimode scheme. The higher power loss in multimode guidance of the pump laser light results in a less efficient operation. Furthermore, the small index contrast between Teflon-AF and aqueous solutions limits the collection angle of the fiber at each segment. The collection angle of TCT compared to PCF will be discussed in Section 2.4.

2.2. Solid core photonic crystal fibers

PCFs, also named microstructured optical fibers, photonic bandgap fibers, and holey fibers, are optical fibers where light confinement and guidance is carried out using a periodic array of air holes (i.e. photonic crystals) instead of a solid cladding. The periodic array of air holes creates an optical bandgap in the cladding that prevents selected bands of frequencies to propagate and escape from the core; thus confining light within the fiber core. In this case, light is said to be confined by the photonic bandgap effect. This scheme for confinement in PCF has been demonstrated for applications in telecommunications [48], supercontinuum generation [48,49], high power delivery [50,51], non-linear optics [52], comb generation [53], and optical sensing [49,54–57] since PCF's first practical demonstration in 1998 by Russell et al. [58,59].

Solid Core-PCF (SC-PCF) is a sub-class of PCF in which the core of the PCF is solid silica. When the liquid of interest is infiltrated into the air cladding holes of SC-PCF, Raman scattering can be obtained through interactions with the evanescent field of the pump laser light guided in the solid core of the fiber. Since the bandgap of the photonic crystal cladding is tunable through its geometry, SC-PCF enables propagation of the pump laser light throughout the fiber length while confining liquids or gases with low refractive indices in the air cladding holes of the fiber. In addition, proper design of the PCF structure (i.e. size and shape of the solid core, and ratios of cladding hole diameter to spacing) enables single mode guidance of light at any optical frequency, known as endless single mode guidance property [60–62].

Pristinski et al. demonstrated the use of SC-PCF, with lengths ranging from 34 to 60 cm, to enhance the retrieved Raman signal of acetonitrile solutions using a 50 mW Ar-ion laser (wavelength of 488 nm) [63]. In addition, it was shown that the ratio of the background Raman signal from the silica core of SC-PCF to the acetonitrile solution remained constant with varying fiber length and laser power. This demonstrated that the Raman signal of silica could be used as an internal reference in which quantitative Raman measurements could be obtained using SC-PCF. Other workers have also demonstrated enhancement in the retrieved Raman signal of 4-mercaptobenzoic acid [64] and R6G [65,66] using evanescent fields in SC-PCF.

The main drawbacks of SC-PCF for Raman spectroscopy lie in the solid core of the PCF. First, as the pump laser light is guided through the solid core of the PCF, unavoidable Raman response of the solid core could be very strong and may overlap with Raman signals of the liquid in the cladding. As most PCFs are fabricated from silica, the strong Raman response of silica below 1100 cm^{-1} (Fig. 3) could interfere strongly with the Raman modes of the liquids under analysis. Second, Raman scattering of the liquid examined is generated through light–matter interaction with the evanescent field of the pump laser. This limits the pump available for Raman scattering. Furthermore, Raman scattering generated in the air holes at the outer regions of the SC-PCF is less confined due to leakage, than what is generated at the inner rings resulting in an additional loss of the retrieved Raman signal. The small air cladding holes of the PCF (i.e. typically on the order of a few microns) also limit the size of the analytes that could be used for Raman analysis. Controllable uptake of analyte solutions into such small air cladding holes also remains a difficult task for long fiber strands.

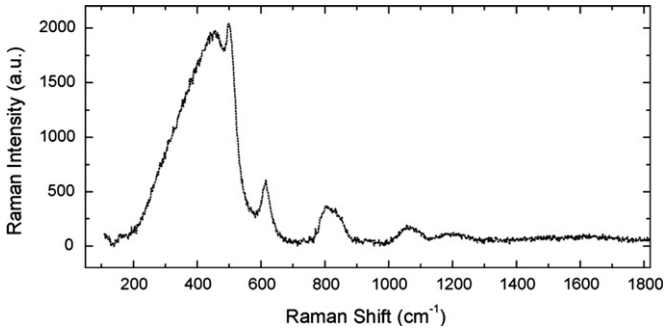

Fig. 3. Raman response of silica.

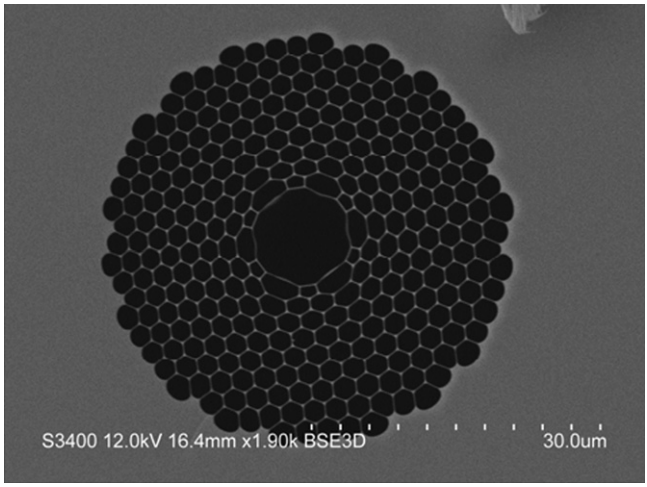

Fig. 4. Scanning electron microscope (SEM) image of a HC-PCF.

2.3. Liquid filled hollow core photonic crystal fibers

Hollow Core-PCF (HC-PCF) is another sub-class of PCF where the core of the PCF is air-filled (Fig. 4). The air core of HC-PCF is usually formed by removing seven or 19 air holes from the cladding of the PCF during the "stack-and-draw' procedure of the fiber fabrication process [67]. The simplest way to utilize HC-PCF for Raman analysis is to fill liquid of interest into both the central air core and the air cladding holes of the HC-PCF. Then, focus the pump laser light into the liquid core of the PCF to generate Raman signals emanating from the liquid.

Recently, Yang et al. have demonstrated for the first time quantitative determination of glucose in the physiological concentration range (0–25 mM) using Raman spectroscopy with liquid filled HC-PCF [68]. Using an 8-cm-long HC-PCF filled with glucose Raman spectra were obtained using a 633 nm excitation source with ~2 mW of laser power and 30 s of integration time. The major Raman peaks of glucose at 1065, 1127, and 1459 cm^{-1} were observed at concentration as low as 1 mM. Naji et al. have also demonstrated efficient Raman scattering in HC-PCF, with lengths ranging from 3 to 9.5 cm, filled with ethanol [69]. A syringe needle with the bottom sealed with a glass cover slip was used as a reservoir for ethanol. HC-PCF was inserted into the needle hole of the syringe needle and dipped into ethanol for filling of the PCF holes through capillary action. The reservoir ensured that ethanol was replenished when ethanol was evaporated. With 100 mW of a 785 nm excitation source, a clear ethanol spectrum was obtained from HC-PCF strands as short as 3 cm. The enhancement factor of the retrieved ethanol Raman signals was 40 times using the maximum HC-PCF length of 9.5 cm [69].

Using liquid-filled HC-PCF over SC-PCF is more advantageous because the former enables direct interaction between the analyte(s) and the pump laser light, which is a stronger and more efficient interaction process than using the evanescent field. Moreover, a larger pump-liquid overlap is achieved as the liquid is confined in the central air core of the HC-PCF where the pump laser is also confined and guided through the fiber. Enhancement of the retrieved Raman signal could be observed for PCF lengths as short as 2 mm where no post-processing of the PCF is required to couple light and fill liquid into the PCF [70]. Furthermore, the advantage of the tunability of the bandgap with the PCF geometry and the possibility of utilizing the endless single mode of operation are also applicable to HC-PCFs [71].

However, as both the central air core and the cladding air holes of the PCF are filled with the liquid of interest, the refractive index contrast between the central core and the average index of the cladding is reduced. Thus, light confinement through TIR could be diminished in this configuration. Moreover, when the index contrast between the liquid and the silica sidewalls of the PCF cladding is small, the bandgap in the PCF cladding also narrows or even disappears [72]. Therefore, light guidance with photonic bandgap effect could also be reduced in this configuration. Furthermore, the bandgap of the HC-PCF is also shifted when the air cladding holes are filled with liquid. Xuan et al. and Antonopoulos et al. demonstrated experimentally the frequency shift of the HC-PCF's bandgap when liquids of different refractive indices were filled in both the central core and cladding holes of a HC-PCF [73,74]. Antonopoulos et al. also derived an equation in which the shift of the PCF's bandgap could be predicted by knowing the refractive index of the liquid filled into the PCF. Further, de Matos et al. demonstrated a novel technique in which different liquids could be used to fill in the central core and the air cladding holes to

obtain the required core-cladding index contrast for TIR operation [75]. Single-mode guidance was also demonstrated for a proper choice of liquids [75].

2.4. Liquid core photonic crystal fibers

Another method to utilize HC-PCF for Raman spectroscopy is to selectively fill the liquid of interest into only the central air core of the HC-PCF. By leaving the cladding air holes intact, the photonic bandgap of the cladding is preserved. The index contrast between the central core and the PCF cladding is also maximized as the average refractive index of the PCF cladding maintained close to 1 due to the high air-filling fraction of the PCF, which enables a strong TIR mode of light confinement. Therefore, selectively filled HC-PCF effectively enables light confinement with both TIR and photonic bandgap effect, which is the distinguishing feature of this technique. By utilizing both light confinement mechanisms, a stronger confinement of the pump laser light and the Raman scattering signal is achieved. In addition, the coupling efficiency of the pump laser light and the Raman scattering signals in TIR modes are improved with a larger collection angle (NA) for the scattered signal.

The acceptance angle of a liquid-core waveguide (LCW) operating in the TIR mode can be described as follows according to [76]

$$\Omega_{\text{cone}} = \pi\left(n_{\text{core}}^2 - n_{\text{eff}}^2\right) \tag{1}$$

where n_{core} and n_{eff} are the refractive indices of the liquid inside the PCF core and the effective index of the PCF cladding, respectively. Table 1 shows an example of the collection angle for TCT and HC-PCF selectively filled with water. The acceptance angle of HC-PCF is nearly five times of that in TCT; thus, HC-PCF provides a stronger confinement of light than TCT.

With liquid core HC-PCF, Han et al. were able to detect a 1% aqueous solution of ethanol (v/v) using a 30-cm-long HC-PCF with 2.1 mW of a 633 nm laser and an acquisition time of 20 s [78]. Huo et al. also reported a 20 times enhancement of Raman signals for glycerol solutions selectively filled into a 2.5-cm-long HC-PCF and detected with an Argon ion laser (514 nm) with 1 mW power and 10 s of integration time [79]. Recently, we have also successfully characterized different nanostructures and biological molecules with liquid-core-HC-PCF-assisted Raman spectroscopy. These included ZnO nanoparticles [54], CdTe nanoparticles [56,80], gold nanoparticles, and DNA fray wires [55,81]. Experimental details and results will be discussed further in Sections 3 and 4.

The main challenge in producing a liquid core HC-PCF is to selectively fill the analyte(s) in question into only the central air core of the PCF. There are two methods to achieve this. One technique is to submerge the HC-PCF into the UV curable gel where the gel can fill both the central air core and the cladding holes of the PCF through capillary

Table 1
Acceptance angle of TCT and HC-PCF selectively filled with water.

Fiber	n_{core} (Water)	n_{eff}	Ω_{cone}
TCT	1.33	1.29 (Telfon)	0.33
HC-PCF	1.33	~1.14 (HC-800 model) [77]	1.47

action [82]. However, since the cladding holes are much smaller than the central air core in the HC-PCF, the gel will fill deeper into the PCF cladding than the central air core. The difference in the filling depth then provides a length in which only the cladding holes are blocked with the gel when it is cut after the gel is UV-cured. The challenge in this technique is that it is difficult to ensure the UV gel is filled into all the cladding holes and to determine the length in which the UV gel is filled.

A faster and more controllable technique is to use a fusion splicer [54]. With the proper parameters, the heat gradients generated from the electrodes in a fusion splicer can collapse the cladding holes of the HC-PCF at its tip while leaving the central core open. Fig. 5 shows the optical image of a HC-PCF before and after its cladding holes were collapsed with a fusion splicer. The optical image shows that the cladding holes can be completely closed while leaving the central core open. Cordeiro et al. have also demonstrated the use of a fusion splicer to create a lateral access to cladding holes in SC-PCF and the central air core in HC-PCF for the practical need in sensing applications including Raman spectroscopy [83].

For both SC-PCF and HC-PCF, cleaning the central core and/or the cladding holes to reuse the fiber also remains a challenge. We found that HC-PCF filled with methanol or IPA could be cleaned by flushing water through the PCF with a miniature diaphragm

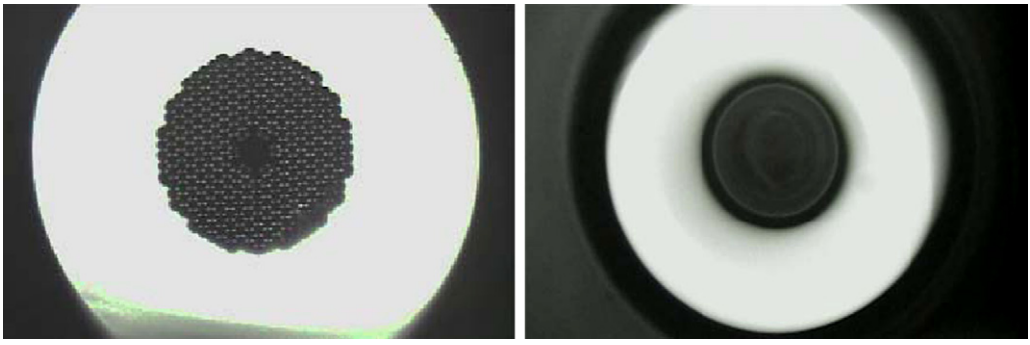

Fig. 5. Optical image of HC-PCF before (left) and after (right) its cladding structure was collapsed using a fusion splicer.

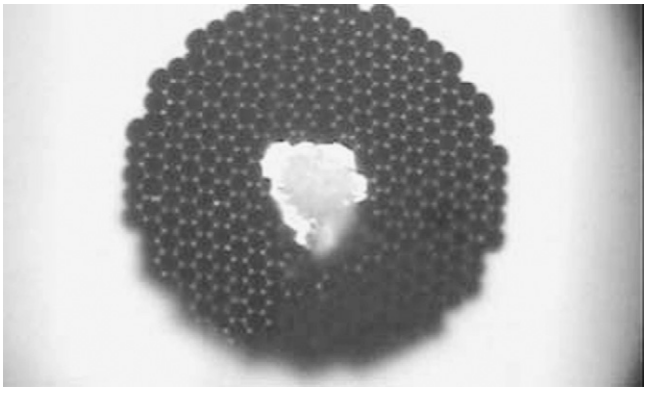

Fig. 6. Optical image of HC-PCF clogged with nanoparticles in the central core.

vacuum pump or a syringe pump [77]. However, for HC-PCF filled with nanoparticles, PCF could not be cleaned due to aggregation of the particles in the pores, likely due to electrostatic charges between the particles and the PCF sidewalls (Fig. 6). It is worth noting that this aggregation was only seen near the top facet of the HC-PCF. The PCF appears clean under a microscope when the tip of the HC-PCF (i.e. ~8 mm) was removed. Nevertheless, refilling the PCF core with capillary action after it was used was difficult to achieve.

2.5. Experimental comparison of optofluidic devices for Raman spectroscopy

In this section, the performance and constraints of Raman spectroscopy will be compared between conventional techniques (i.e. cover slide) and some of the different optofluidic platforms described in the previous sections; including TCT and HC-PCF. By using a simple liquid such as water as a reference, the Raman spectra were obtained using the different techniques for comparison (Fig. 7). Namely, a cuvette, a 20-cm-long TCT (Biogeneral Inc., model AF-2400, core diameter =~120 μm) and a 4-cm-long HC-PCF (NKT Photonics, modeled HC-800, core diameter =~10 μm) with selective (liquid core PCF) and non-selective filling technique (liquid filled PCF) were utilized to obtain Raman spectra of water. Table 2 compares the experimental parameters used in each Raman measurements as well as the amount of sample volume used for each technique and the intensity of the OH stretching mode at ~3400 cm^{-1} from the obtained water spectra.

As shown in Fig. 7 and Table 2, the use of TCT or HC-PCF enables stronger OH stretch modes to be obtained with up to 25,000 times lower sampling volume than the use of a cover slide as used in conventional techniques. If a cuvette (i.e. 3 mL) was used instead, sampling volume would be 750,000 times greater than that in HC-PCF with selective filling. This demonstrated that the use of optofluidic devices enhanced the retrieved Raman

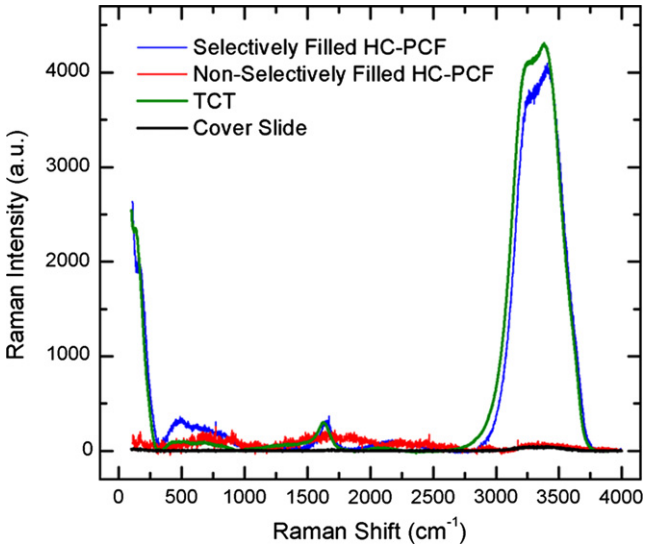

Fig. 7. Raman spectra of water obtained using a cuvette, a 20-cm-long TCT, and a 4-cm-long HC-PCF with selective and non-selective filling.

Table 2
Performance of Raman spectroscopy using a cuvette, TCT, and HC-PCF and their corresponding sample volumes used.

Technique	Length (cm)	Sample Volume (μL)	Pump power (mW)	Laser exposure time (s)	OH stretch mode intensity at 3400 cm^{-1} (Counts)
Cover slide	–	~100	0.17	2	41
TCT	20	~2	8.5	10	4273
Liquid filled PCF	4	~0.004	0.17	2	71
Liquid core PCF	4	~0.224	0.17	2	4026

signal and minimized the required sample volume through strong confinement of both the pump laser light and the analyte(s) in the same fluidic channel.

To compare the performance of different optofluidic devices for Raman spectroscopy, the enhancement factor can be calculated as a figure of merit extracted from the Raman spectra. The enhancement factor can be easily calculated by determining the intensity ratio of a Raman mode obtained using the different techniques. However, a few factors must be normalized between the different measurements or techniques for the enhancement factor to be comparable. These factors include power, or power density, of the pump laser, exposure time of the measurement, and active volume of the measurement, which is defined to be the volume in which there is an overlap between the pump laser and the analyte. A general equation of enhancement factor between different optofluidic techniques in Raman spectroscopy is shown in the following equation:

$$\text{Enhancement Factor} = \frac{\text{Normalized Intensity of Raman Mode obtained with Technique A}}{\text{Normalized Intensity of Raman Mode obtained with Technique B}} \tag{2}$$

From the intensity counts of the OH stretch mode obtained from water using the different techniques as shown in Table 2, the strongest (i.e. most intense) OH stretch modes were obtained with TCT and HC-PCF selectively filled with water. Although the intensity counts of the two OH stretch modes are similar, the length and the core diameter of the HC-PCF are five and 12 times less than that of the TCT, respectively (i.e. the sample volume in HC-PCF was ~1389 times less than that in TCT). The pump laser power and exposure time used in the HC-PCF measurement were also 50 times lower and five times shorter, respectively, than that in the TCT measurement. This gives liquid core PCF an enhancement factor (OH mode intensity from HC-PCF/ OH mode intensity from TCT normalized with the same power, exposure time and volume) of ~327,178 times greater than TCT. Therefore, selectively filled HC-PCF gave the largest enhancement of the retrieved Raman signal of water overall.

This large enhancement from liquid core-filled PCF is expected for two main reasons. First, the core diameter of HC-PCF is only ~10 μm, which is 12 times smaller than that of TCT (~120 μM). The smaller core size provides a stronger (i.e. more intense) fundamental mode at its designed guiding wavelength than the highly multimode guided TCT, enabling a stronger light–matter interaction. Second, a stronger light confinement and a larger collection angle in PCF were achieved with selective-filling due to the presence of two

different light guiding mechanisms TIR and the photonic bandgap effect as discussed earlier in Section 2.4.

The reduction in the efficacy of both guiding mechanisms is the reason why non-selectively liquid filled PCF provided much weaker OH stretch modes than selectively liquid filled core PCF. As water was also filled into the cladding holes of the HC-PCF, the average refractive index of the cladding was lowered towards the water refractive index (i.e. 1.33) due to the high air-filling fraction of the HC-PCF. With water filled into the core of the HC-PCF, the guidance of TIR was significantly weakened due to the small index contrast between the core and cladding of the PCF. In addition, the filling of water into the cladding holes had shifted and narrowed the photonic bandgap of the PCF. Therefore, the photonic bandgap guiding strength of the HC-PCF was also reduced. As a result, a very weak confinement and collection of the pump laser and scattering photons were achieved with non-selective filling. A stronger confinement and collection efficiency in liquid core PCF enables a larger enhancement factor of the Raman signals to be obtained as we demonstrated. This large enhancement enables us to observe many more clear and strong Raman modes from simple chemicals, such as methanol (Fig. 8) [77], as well as more complicated materials, such as nanostructures and biological molecules which will be discussed in Sections 3 and 4. Furthermore, HC-PCF significantly reduces the limit of detection in Raman spectroscopy. For example, we demonstrated that with a strand of 30-cm-long TCT, the limit of detection for 1-naphthalenethiol (NPT) in methanol was 500 μM [77]. However, with a 15-cm-long HC-PCF selectively filled with nanoparticles, the limit of detection was significantly reduced to only 10 μM.

One advantage of utilizing fiber-based optofluidic mechanisms for enhancing the retrieved Raman signal is that the interaction length can be increased with increasing fiber length. Recently, we have demonstrated and compared experimentally the increasing enhancement with extended fiber length for TCT and HC-PCF [77]. The red dots in Fig. 9 show the normalized intensity of the OH stretch mode (at ~3400 cm^{-1}) from water at

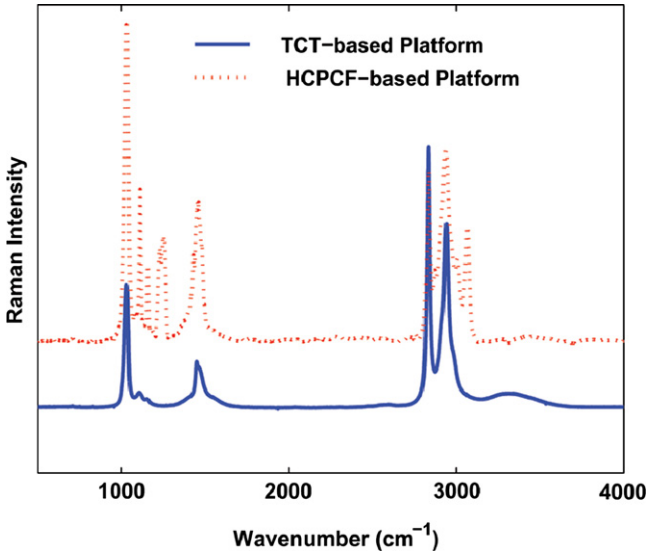

Fig. 8. Raman spectra of methanol obtained using TCT, and HC-PCF with selective filling.

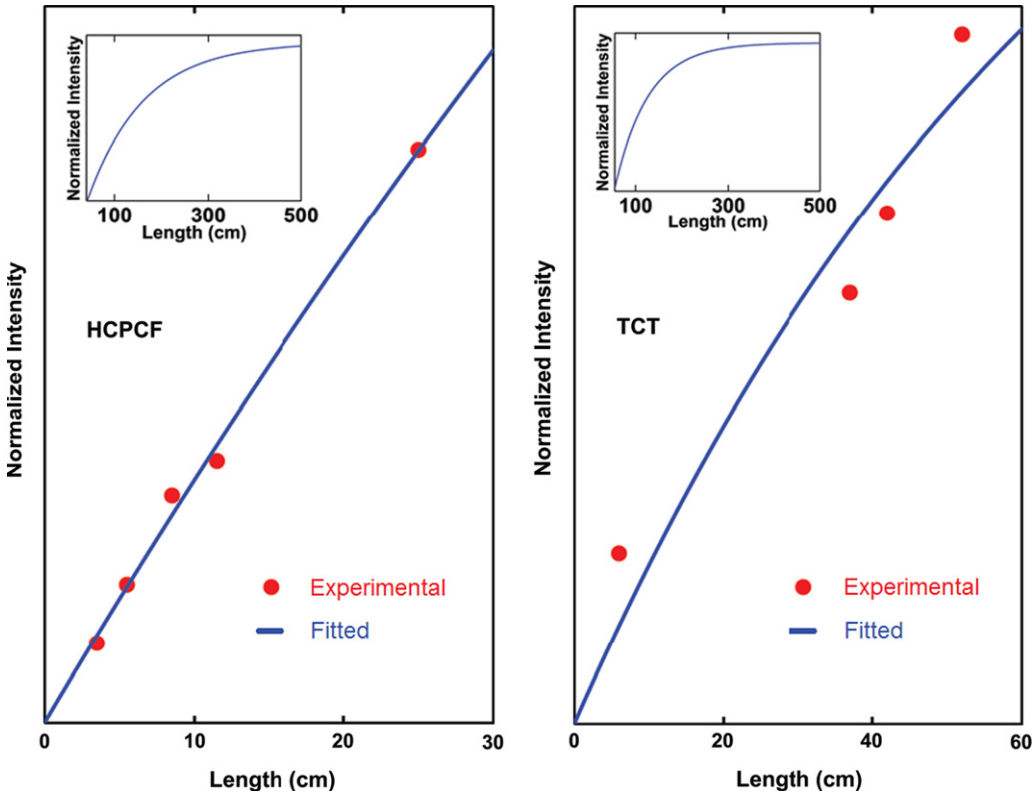

Fig. 9. Normalized OH stretching mode intensity at ~3400 cm^{-1} with varying length of HC-PCF and TCT. Blue line shows the result fitting Eq. (3) to the experimental data. The intensities are normalized with respect to the intensity obtained with a cuvette. Insets: predicted plateau of intensity for the LCW over fiber length of 500 cm. (For interpretation of the references to color in this figure caption, the reader is referred to the web version of this article.)

different fiber lengths up to 25 and 50 cm long for HC-PCF and TCT, respectively. The intensity in the figure was normalized to the intensity obtained from a cuvette. As shown in Fig. 9, the normalized intensity for both HC-PCF and TCT increases with increasing fiber length for the practical range of fiber length utilized. The increases in Raman signal with fiber length were due to increased light–matter interaction inside the prolonged fiber. However, due to attenuation within the fiber (i.e. absorptions from the fiber and the sample), the increase of Raman signal will gradually reduce and eventually plateau. This suggests that there is a maximum length in which we can utilize an optofluidic fiber to enhance the retrieved Raman signal.

Utilizing the model from LCW with backscattering configuration [84], we were able to fit the OH stretching mode intensity obtained experimentally from different fiber lengths and predict the length of fiber at which the maximum enhancement is achieved. In the LCW model, the intensity of the Raman signal in the backscattering configuration is

$$I_{LCW} = \frac{\kappa}{2}\left(1-e^{-2\alpha L}\right) \tag{3}$$

where α is the loss coefficient of the fiber and L is the length of the fiber used for Raman measurement. κ is a defined parameter in which $\kappa = P_o \rho \sigma \pi NA$, where P_o is the pump laser power coupled into the fiber, ρ is the Raman cross-section of the solution, σ is the number of scattering center per sample volume and NA is the numerical aperture of the fiber. Using two parameters α and κ, we were able to fit the experimental results closely with the model as shown in the blue line in Fig. 9. If we extend the fitted line to fiber length of 500 cm (as shown in inset of Fig. 9), we determined that the intensity of the Raman signal reaches a plateau at ~500 cm in HC-PCF and ~300 cm in TCT. This shows that HC-PCF not only provides a greater enhancement of the retrieved Raman signal than TCT with a short fiber length as shown in Figs. 7 and 8, it can potentially provide a greater maximum enhancement than TCT through a longer length of fiber. The greater maximum enhancement can be understood through a longer propagation length of the HC-PCF. It was found from the fitted result that the propagation length, α^{-1}, was 144 cm for TCT and 267 cm for HC-PCF. The propagation length of HC-PCF was almost twice that of TCT which implied that HC-PCF has much lower losses within the fiber; therefore, enabling more light–matter interactions with a prolonged fiber strand. Thus, a greater maximum enhancement could be achieved with HC-PCF.

3. Characterizing colloidal nanostructures

In the last two decades, there has been a tremendous interest in synthesizing nanometer-sized semiconductor and metallic structures suspended in solution [85–89]. These novel colloidal nanostructures possess intriguing optical properties of quantum-confined particles as well as practical advantages of solution-based processing. Advancements in synthesis techniques have enabled simple and cost-effective ways of synthesizing small, monodisperse and water-soluble nanostructures with different shapes for a wide range of novel applications including optoelectronics [90], photovoltaics [91], bio-sensing [92], bio-imaging [93], as well as cancer treatments [94].

The current challenge in developing more advanced and complex nanostructures is a cost-effective, reliable and sensitive technique to monitor and control the physical, chemical, shape and size-dependent properties of nanostructures before, during, and after their fabrication on a nanometer scale. Although there are many analytical techniques which are currently available and more which are currently being deployed to characterize the different properties of nanostructures, these techniques provide information only on the composition and certain macroscopic properties of the nanostructure. For example, photoluminescence (PL), electroluminescence (EL), ultraviolet-visible (UV–vis) spectroscopies provide the optical and electrical characteristics of the nanostructure. Transmission electron microscope (TEM) or high resolution TEM (HR-TEM) provides the physical image of the nanostructure. Capillary zone electrophoresis (CZE), X-ray diffraction (XRD), and X-ray photoelectron spectroscopies (XPS) provide information on the ions, crystalline and composition of the nanostructures, respectively. Nevertheless, these techniques do not describe how the core of the nanostructures interact with the stabilizers and ligands adsorbed or conjugated on the surface of the structures. The impact of the interactions on the overall molecular structure, molecular complex and different properties of the nanostructures also remained unclear which limits our ability to improve the performance and functionalities of the different nanostructures for the different applications.

With the novel development of optofluidic technology in recent years, resolving detailed structural information of the nanoparticles became permissible through measuring their native Raman modes. In this section, we discuss examples of such optofluidic systems that enable the measurement of native Raman modes of semiconductor and metal nanoparticles.

3.1. Semiconductor nanoparticles

Colloidal semiconductor nanoparticles are a type of material characterized by a semiconductor core that has a diameter on the nanometer scale, and is capped or stabilized by a surrounding material (often a ligand, polymer, or organic molecule). Semiconductor nanoparticles are of keen interest in a wide variety of optical, electrical, magnetic, and biomedical applications. What distinguishes them from more traditional bulk semiconductors is their capability to selectively tune the electronic bandgap energy levels and colors based on the size of the nanoparticles alone. The nanoparticle characteristics and size are based on the growth conditions and recipe of the wet chemistry synthesis. Not only is the semiconductor core important to the characteristics of the nanoparticle, but so is the capping material that can be tuned for various applications as well. It is therefore critical to be able to characterize both the core and capping material, and if desired, manipulate the synthesis process in order to develop precisely tuned nanoparticles for a specific application.

We have recently demonstrated the capabilities of Raman spectroscopy to investigate the structural changes of ZnO nanoparticles during their growth process [54]. Aliquots of ZnO solutions were sampled and studied at four key steps in the fabrication procedures. Obtaining information at different phases in the growth process allows for more in-depth analysis of the specific growth mechanics of the nanoparticles. While over 99% of the sample is composed of water, with the use of a hollow core waveguide to enhance the light–matter interaction, Raman vibrations from the chemicals used were clearly identifiable on the millimolar level. Fig. 10 is an overlay of the Raman spectra obtained at each shift and highlights modes that correspond to important Raman modes. By assigning the changes in spectra to associated modes of the capping polymer, the specific effects that the UV radiation has on the nanoparticle growth process can be explored and improved.

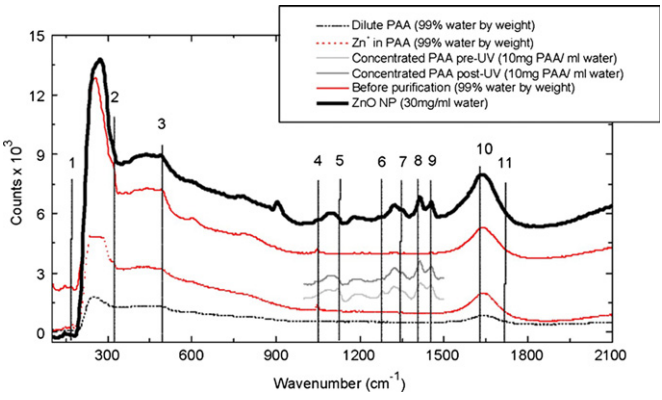

Fig. 10. Overlay of Raman spectra obtained at different stages throughout the nanoparticle growth.

This investigation involved using several aliquoted samples to be investigated during the growth process itself to demonstrate the effectiveness of Raman spectroscopy in analyzing the growth mechanisms of ZnO nanoparticles. This study demonstrated the potential to provide real-time feedback as to the status of the nanoparticles when sampling is implemented in situ during the growth process in effect. This provides immediate feedback and allows for growth parameters to be adjusted in order to create the desired final product.

In addition to the Raman analysis of ZnO nanoparticles, HC-PCF-assisted Raman spectroscopy was used to analyze the effects of post-growth annealing on CdTe nanoparticles [80]. It was immediately evident that rapid thermal annealing was affecting the CdTe nanoparticles by the observed changes in the collected Raman spectra, as shown in Fig. 11.

The grossly changing modes in the sample were determined to be from the semiconductor core of the nanoparticles rather than from the capping ligand and were assigned to both desired CdTe modes at ~140 cm^{-1} and 165 cm^{-1}, and undesired Te defect modes at ~127 cm^{-1} and ~141 cm^{-1}. By plotting a ratio of the modes emanating from the Te defects to the CdTe mode at 165 cm^{-1} as shown in Fig. 12, it is clear that a significant transition of crystal structure occurs above 300 °C which results in the reduction of the amount of Te defects in the core.

These changes were verified through the use of XRD, a commonly used technique to analyze crystal orientations of semiconductors. The XRD results obtained are shown in Fig. 13. From the XRD results, it can be determined that both unannealed CdTe and CdTe annealed at low temperature, the semiconductor core possesses both wurzite and zincblende forms of CdTe. The narrowing peak with annealing at 400 °C confirms what was suspected from the Raman analysis: the CdTe core coalesces into a single wurzite crystal form, with fewer Te defects across grain boundaries of different crystal structures.

What is of key importance in this study is the enhanced Raman signal, which enables more accurate analysis of the Raman modes required to detect this change in crystallinity.

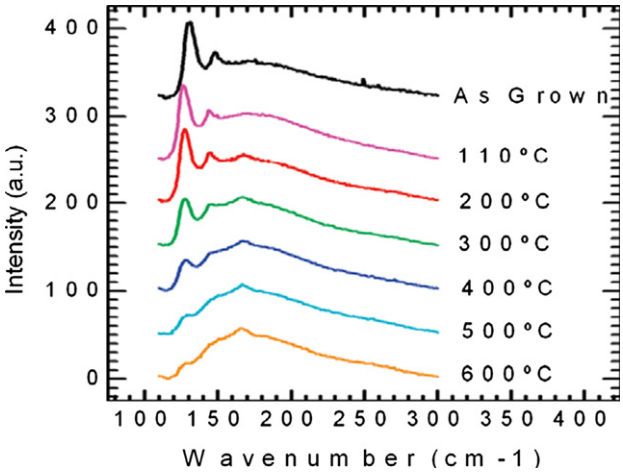

Fig. 11. Overlay of Raman spectra obtained of the CdTe nanoparticles with respect to rapid thermal annealing temperature changes.

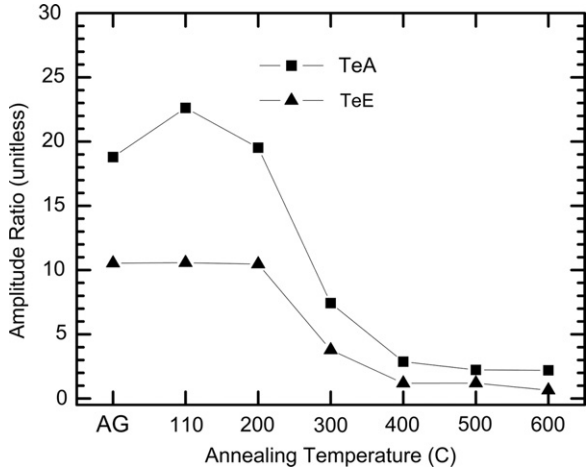

Fig. 12. Ratio of Te defect modes to the desired CdTe mode at 165 cm^{-1}.

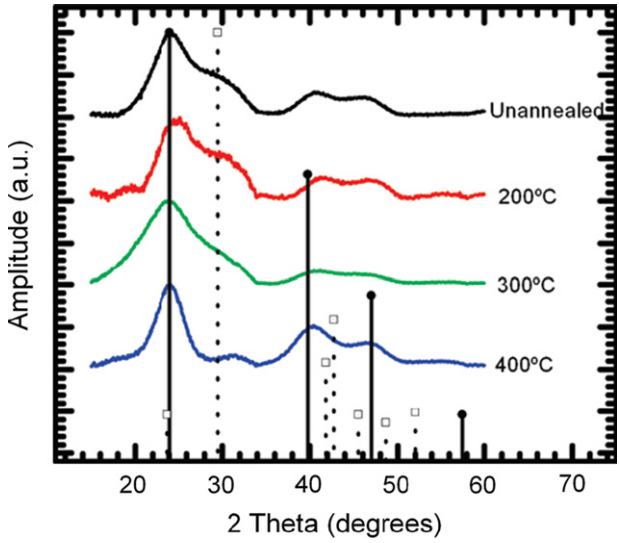

Fig. 13. XRD data indicating the change in crystalline structure of the nanoparticles due to rapid thermal annealing.

Conventional Raman spectroscopy does not provide the required sensitivity to resolve the nanoparticle modes due to the small size of the individual nanoparticles (on the scale of 3–5 nm) and that their core is surrounded by a polymer encapsulation. Moreover, these nanoparticles are diluted in aqueous solutions. With the enhancement in the retrieved Raman signal through HC-PCF-assisted Raman spectroscopy, the required sensitivity was demonstrated to enable the detection of the nanoparticle modes. An alternative method to analyze changes in the crystal structure of nanoparticles is XRD, which is time consuming, incompatible with materials in their as-grown solution form, and ultimately destructive as well. With the use of HC-PCF, the effectiveness of Raman spectroscopy for

characterization of semiconductor nanoparticles and their capping material has been demonstrated and can operate both as a supplement to traditional characterization and, in some cases, as a facile alternative.

Recently, we have also successfully obtained, for the first time, clear Raman spectra of colloidal CdTe quantum dots (QDs) stabilized with different thiol ligands using liquid filled HC-PCF [56]. Strong and clear Raman modes of the CdTe semiconductor core, capping ligands, and their interfacial structures were successfully observed at a QD concentration similar to that during the synthesis process without any metallic nanoparticles integrated for enhancement. The obtained Raman modes were further correlated to and compared with different properties of the QDs including photoluminescence (PL) efficiency, stability, solubility, and capability for bioconjugation [56].

CdTe QDs with sizes of ~3–4 nm were stabilized with thioglycolic acid (TGA), 3-mercaptopropionic acid (MPA), or 1-thioglycerol (TG) and gave a PL peak between 525 and 560 nm after synthesis. The structure of the three thiol agents is shown in Fig. 14. By selectively filling the aqueous QD solutions into the central core of a HC-PCF, Raman spectra with peak correlated to the different parts of the QD structure were obtained (Fig. 15).

In the lower Raman shift region, between 100 and 200 cm^{-1}, Raman modes corresponding to the QD core were obtained. The peaks at ~120, ~140 and ~160 cm^{-1} are attributed to the Te A_1, Te E and CdTe TO, and CdTe LO modes of the QDs, respectively [95–99].

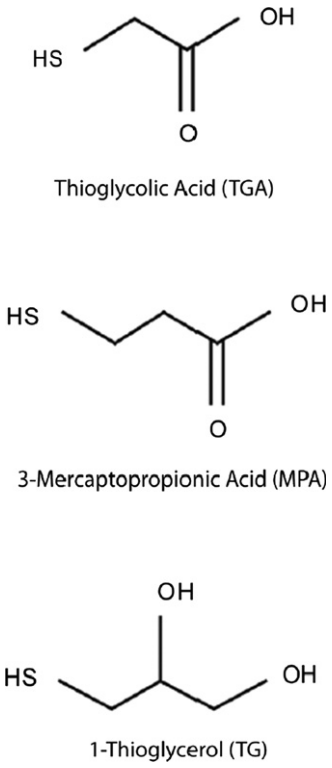

Fig. 14. Three thiol agents for CdTe QD stabilization.

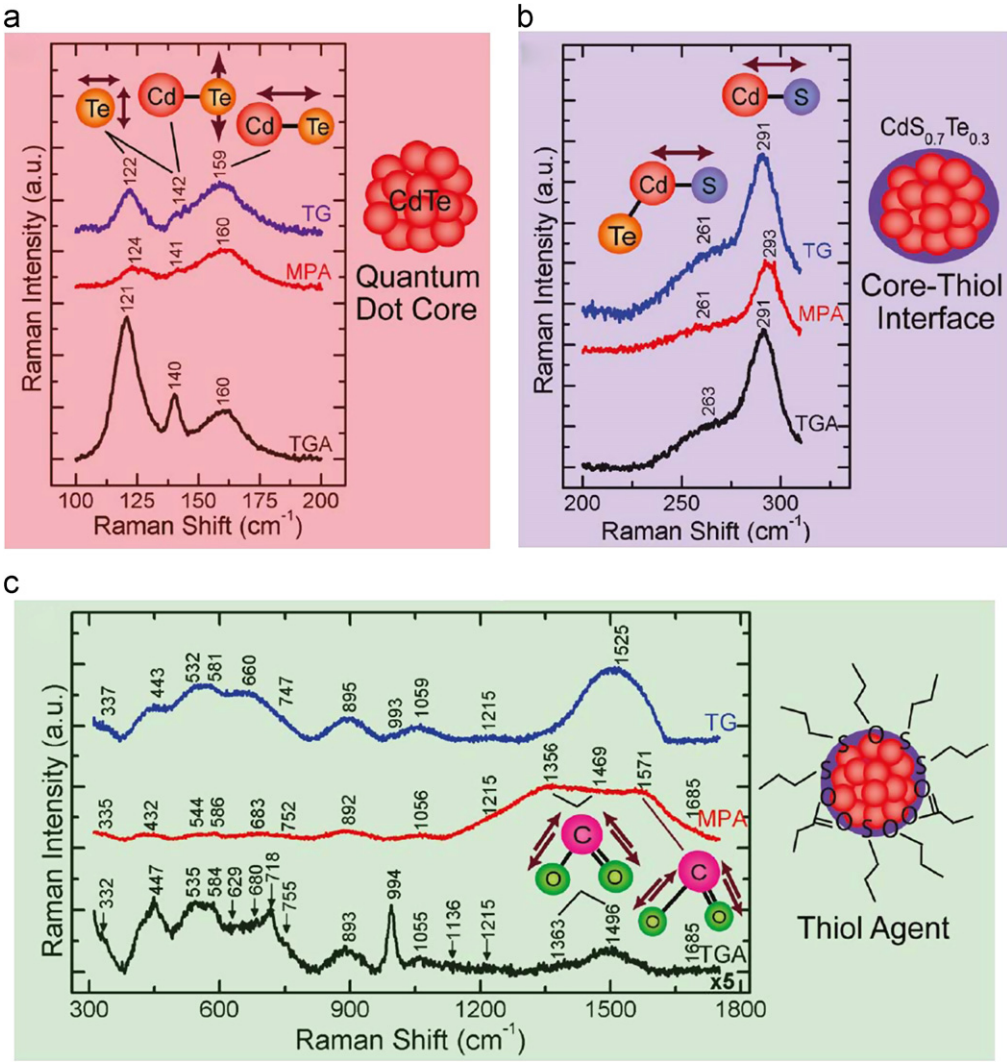

Fig. 15. Raman spectra of aqueous CdTe QDs stabilized with TGA, MPA or TG. The Raman spectra were divided into three regimes (a) 100–200, (b) 200–310, and (c) 310–1750 cm^{-1} in which the Raman modes of the QD core, core–thiol interface, and thiol agents of the QDs were observed, respectively.

Similar to our previous study on CdTe nanoparticles that were processed with RTA, these modes indicated that both the crystalline CdTe core and Te defects were present in the QDs. Moreover, as these three modes were obtained in all three spectra of the QDs with different thiol agents, they showed that crystalline CdTe core and Te defects were present in the QDs regardless of the type and structure of the capping agent used.

To compare the crystallinity of QDs stabilized with different thiol agents, the intensity ratio of the Te A_1 mode to the CdTe LO mode was calculated (Table 3). Table 3 suggests that crystallinity improved from TGA-capped QDs to TG-capped QDs and is greatest with MPA-capped QDs. The improved crystallinity contributes to a greater PL efficiency with

fewer trap states that led to non-radiative processes; thus, a brighter QD was synthesized with MPA.

In the mid-Raman shift region, between 200 and 310 cm^{-1}, Raman modes corresponding to the interactions between the QD core and the thiol capping agents were observed. The two peaks at ~291 and ~260 cm^{-1} shown in this region are ascribed to the surface optical phonon (SO) mode of the CdS compound [100,101] and CdS-like LO phonon mode of the ternary CdS_xTe_{1-x} compound, respectively [102,103]. The two CdS-related modes suggested that Cd ions on the surface of the QD core were bonded with the S ions in the thiol terminus of the capping agents, after breaking the S–H bonds in the thiol group, for stabilization. Several other studies have also proposed the same interaction between the thiol group and the core of the QDs [89,104,105].

Since no visible CdS LO mode at ~300 cm^{-1} is observed in the spectra, the CdS shell had not formed around the CdTe cores in the three QD solutions. Instead, the Raman mode at ~260 cm^{-1} indicated that $CdS_{0.7}Te_{0.3}$ was formed in all three QD samples with the different thiol stabilizing agents. The rich S content in the alloys indicated that many thiolates were coupled with the CdTe cores and formed a CdS shell-like system, which showed that thiolates were strongly passivating the surface of the QDs and stabilizing the QD core. Strong surface passivation also eliminated surface defect states which contributed to a greater PL efficiency. In addition, since the three thiol agents have different chain lengths, the formation of the $CdS_{0.7}Te_{0.3}$ in the three QD solutions also suggested that the degree of surface passivation could be unrelated to the length of the thiol chain bonded to the QD surface.

No S–S vibrational modes were observed between 480 and 510 cm^{-1} which indicated that QDs were not photo-oxidized. This is because photo-oxidation of the surface thiol agents could catalyze the formation of disulfides through breaking the Cd–S bonds and reacting with a neighboring thiol group [106,107]. The strong surface passivation and the absence of photo-oxidization observed from the mid-Raman shift region demonstrated that the CdTe QDs capped with TGA, MPA and TG are all highly stable in their native aqueous environment.

In the high-Raman shift region, between 310 and 1750 cm^{-1}, Raman modes corresponding to the different thiol agents were observed. In particular, Raman modes in this region showed that the carboxylate terminal of the thiol agent (i.e. the opposite end to the thiol terminal) were also interacting with the CdTe core and provided further stability to the QDs. These modes are the symmetric and asymmetric stretching modes of the carboxylates observed between 1330 and 1500 cm^{-1} and between 1570 and 1580 cm^{-1} in TGA and MPA-capped QDs, respectively [89,105,108]. These modes indicated that the carboxylic acid groups were adsorbed onto the QD surfaces as carboxylates, most likely by forming bonds with the Cd ions on the CdTe core.

Table 3
Intensity ratios of the Te A_1 mode to CdTe LO mode for CdTe QDs stabilized with different thiol agents.

Intensity ratio	TGA	TG	MPA
Te A_1 / CdTe LO	2.949	0.901	0.499

Carboxylate ions may coordinate to a metal in three modes, namely, unidentate, bridging bidentate and chelating bidentate [108, 109] [108,109] . Through calculating the wavenumber separation between the symmetric and asymmetric stretches of the carboxylate mode, it was found that both TGA and MPA-capped QDs showed the formation of chelating bidentate complexes. In addition, TGA formed the bridging bidentate complexes while MPA formed the unidentate complexes.

Table 4 shows the calculated intensity ratios of the COO^- symmetric stretches to the CdS 2SO mode. The large ratio in MPA-capped QDs implied that a large quantity of carboxylate ions are coordinated with the Cd ions. This is not only suggesting that the formation of carboxylate–metal complexes is much more favorable with MPA than TGA, probably due to the longer chain length of MPA than TGA, but also that the surface of the QD is more passivated by carboxylates in the MPA chain [110,111]. As a result, MPA-capped QDs contained fewer defects and higher PL quantum efficiencies, with potentially lower solubility and bioconjugation capabilities since fewer free carboxylate ions are available. Since the chelating bidentate interactions of the carboxylate–metal complexes are stronger than the unidentate interactions of the thiolates–metal complexes, the larger quantity of chelating bidentate complexes formed in MPA-capped makes it more stable than the TGA-capped ones.

With enhancement in the retrieved Raman signal from HC-PCF-assisted Raman spectroscopy, strong and clear Raman modes from thiol-capped CdTe QDs were obtained for the first time. With these strong Raman modes, it was confirmed that CdTe QDs were formed. Moreover, MPA and TGA interacted and stabilized the QD core through both terminals of its molecular chain while TG only bonded with the QD core through its thiol end. MPA-capped QDs were also found to have more carboxylate–metal complexes formed than TGA-capped QDs which provided a stronger QD stability but potentially lower solubility and capability for bio-conjugations.

3.2. Gold nanoparticles

With advancements in colloidal synthesis and nanofabrication techniques in the past few decades, there has been tremendous interest in synthesizing nanometer-sized probes using metallic nanoparticles for biological and medical applications such as drug and gene delivery [112–114], bio-sensing [115], bio-diagnostics [116], and bio-imaging [117]. Metallic nanoparticles, such as copper, silver, and gold are known to provide significant enhancements in the local electromagnetic (EM) field around the particle due to excitation of surface plasmon polariton (i.e. the oscillation of electron clouds induced by photon energy) [118,119]. In the case of metallic particles at the nanometer scale, electrons are

Table 4
Intensity ratios of the symmetric carboxylate stretch to CdS 2SO mode for different carboxylate–metal complexes.

Capping agent	Intensity ratio	
	$\nu_s(COO)_1$/CdS 2SO	$\nu_s(COO)_2$/CdS 2SO
TGA	0.205 (bridging bidentate)	0.547 (chelating bidentate)
MPA	12.803 (unidentate)	5.390 (chelating bidentate)

[1] Symmetric stretches between 1300 and 1400 cm^{-1}, [2] Symmetric stretches between 1400 and 1500 cm^{-1}

strongly confined in all three dimensions. As a result, upon excitation of the surface plasmon polariton, the EM field induced by the electrons' oscillation around the particle can be much larger than that from the incident EM field; thus, giving an enhanced localized EM field.

In Raman spectroscopy, metallic nanoparticles have been greatly utilized to enhance the Raman scattering signal. The use of metallic nanoparticles to enhance Raman scattering is known as SERS. It has been demonstrated that metallic nanoparticles can provide an enhancement of the Raman signal by up to 10^9–10^{10} times which enables the detection of a single molecule [26,27,120–123]. In this section, we will discuss how optofluidics can assist in characterizing molecular structures of metallic nanoparticle probes with Raman spectroscopy to improve the synthesis process using only nano-liters of solutions. In Section 5, we will also discuss how we can combine and utilize SERS with optofluidic technologies to achieve enhancements in the detected Raman signal greater than that of SERS or optofluidic technology alone, as well as, greater functionalities for detecting different liquid solutions.

In order to maximize EM enhancements of metallic nanoparticles employed in different applications, several methods of stabilizing and functionalizing the nanoparticles are required. For example, in bio-diagnostics gold nanoparticles can be designed as a probe, or a tag, to target and report, cancerous cells in the human body [116]. However, signal reporting through SERS can only be achieved through proper adsorption of the Raman dye onto the surface of the gold nanoparticle. In many cases, successful dye adsorption is inconsistent with the same synthesis recipes and, similar to semiconductor nanoparticles, there is no effective technique available to determine experimentally how the different ligands, or stabilizers, are interacting with the metal nanoparticle core at the molecular level. Although Raman spectroscopy can provide very specific bonding interactions between ligands and the metallic nanoparticles, conventional Raman spectroscopy techniques are highly limited by its low sensitivity to observe small nanoparticle solutions. Even with milli-liters of nanoparticle solutions and a hundred milliwatt of laser power, a strong and clear Raman spectrum of the nanoparticle may not be obtained. Therefore, it remains a challenge to determine, confirm, and evaluate the bonding interactions from each stabilization and functionalization molecule in the nanoparticle system as well as any time-dependent changes after the synthesis. As a result, it limits our ability to optimize the nanoparticle probe designs as well as the synthesis process to realize and maximize the EM enhancements for the different applications.

In synthesizing SERS probes for biological applications, stabilized gold nanoparticles are often used to adsorb Raman dyes for signal reporting. However, adsorption is often not reproducible and SERS enhanced signal is inconsistent due to the weakening of the gold nanoparticle stability from different storage conditions.

Recently we have demonstrated the use of PCF-assisted Raman spectroscopy to observe binding interactions at the surface of a citrate-stabilized gold nanoparticles used as core nanoparticle for Raman probe synthesis. This enabled monitoring of the citrate–gold interactions which were found to reduce Raman dye adsorption and thus prohibit the generation of the SERS signal. In addition, we observed dynamic changes of the nanoparticle structure through increasing pump laser power where we determined the damage threshold of the synthesized nanoparticle probe.

The metallic nanoparticles being characterized are 60 nm citrate-stabilized gold nanoparticles purchased from Ted Pella Inc. which are used as the base particle for

synthesizing nanoparticle probes for biological applications. To synthesize the nanoparticle probe, crystal violet (CV) was adsorbed onto the gold nanoparticles for reporting purposes. A phospholipid bilayer is then coated around the particles to provide strong biocompatibility through mimicking the cell membrane while stabilizing the gold nanoparticles themselves [124].

The process of CV dye adsorption fails occasionally and is inconsistent. Using a 6-cm-long HC-PCF (modeled HC-1060) purchased from NKT Photonics, a clear and strong Raman spectrum from the citrate-stabilized gold nanoparticle was observed with 0.17 mW of a HeNe laser (633 nm) and <10 nL of nanoparticle solutions. Interactions between citrate molecules and the gold nanoparticle core were also determined. Fig. 16 shows the Raman spectrum obtained from a fresh batch of citrate-stabilized gold nanoparticles in which adsorption of the CV dye was successful and SERS signal was observed (Fig. 17). In particular, the stretching modes of the carboxylates from the citrates between 1380 and 1600 cm^{-1} are of interest here. These carboxylic acid groups are known to form complexes with the gold surface that stabilize the nanoparticle core after deprotonation [125,126]. The Raman modes at 1381, 1445 and 1544 cm^{-1} are assigned to the symmetric stretches of the carboxylate. The mode at 1597 cm^{-1} is assigned to the asymmetric stretch of the carboxylates. Similar to the CdTe nanoparticles discussed in Section 3.1, the wavenumber difference between the symmetric and asymmetric stretch of the carboxylates modes indicates the type of complexes formed between the metal and the carboxylates (i.e. the gold–carboxylate complex in this case).

If the wavenumber difference between the symmetric and asymmetric modes of the carboxylate is greater than those of the ionic values, a unidentate complex is formed. Conversely, if the wavenumber difference is much lower than the ionic values, then a bridging bidentate complex is formed. Lastly, if the wavenumber difference is greater than that of the bridging bidentate and closes to the ionic values, then a chelating bidentate

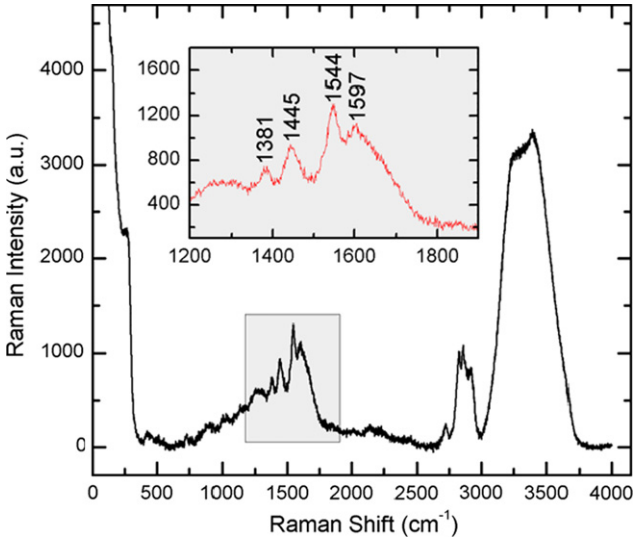

Fig. 16. Raman spectrum of a fresh batch of gold nanoparticles stabilized by citrate. Inset: enlarged spectrum showing carboxylate stretching modes of citrate.

complex is formed. For liquid solutions similar to citrate, the symmetric stretches of carboxylate anion are located around 1414–1425 cm^{-1} where the asymmetric stretch of the carboxylate anion is located around 1560–1580 cm^{-1} [108]. Therefore, the wavenumber difference between the ionic carboxylate symmetric and asymmetric stretching modes is about 145–164 cm^{-1}. With 100 mW of power using RR with an Argon ion laser (514.5 nm), Munro et al. also observed carboxylate symmetric stretching modes between 1400 and 1575 cm^{-1} from citrate-stabilized silver nanoparticles using approximately 2 mL of the colloid, which is about six orders of magnitude larger in volume and about five times greater power than with HC-PCF [125].

Table 5 shows the wavenumber position of the symmetric and asymmetric stretching modes of carboxylate, their respective intensity ratio to the carboxylate asymmetric stretch, wavenumber differences, and proposed complexes according to the discussion above. The table shows that one carboxylic group of the citrate is ionic which means that it did not form a complex with the nanoparticle and was exposed on the surface. In addition to the carboxylate anions, citrate formed unidentate and bridging bidentate complexes with the nanoparticle core. This finding correlates with the proposed interactions of Munro et al. in which two of the three carboxylic groups interact with the citrate-reduced colloid and the third group is exposed on the surface observed from their SERS data [125]. Therefore, fresh gold nanoparticles used in this experiment were stabilized strongly by

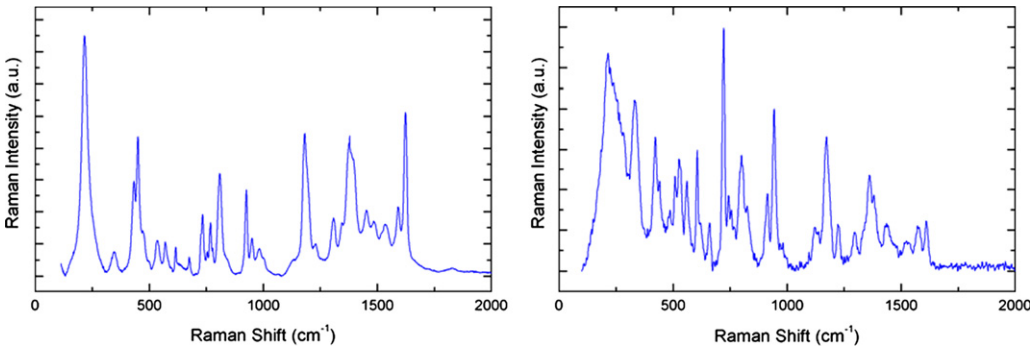

Fig. 17. SERS spectrum of Raman probe with CV adsorbed on its surface (left) obtained using a 633 nm laser with 0.17 mW power and a selectively filled HC-PCF and (right) 785 nm laser with 80 mW power. Raman probe was synthesized using a fresh batch of gold nanoparticles stabilized by citrate.

Table 5
Wavenumber position of the symmetric and asymmetric stretching carboxylate modes of citrate, their intensity ratio to ν_{as}(COO), respective wavenumber differences and proposed complexes for a fresh batch of citrate-stabilized gold nanoparticles.

ν_s(COO)	ν_{as}(COO)	Intensity ratio of ν_s(COO) to ν_{as}(COO)	Wavenumber separation between ν_s(COO) and ν_{as}(COO) (cm^{-1})	Proposed structure
1381	1597	0.474	216	Unidentate
1445	1597	0.867	152	Ionic
1544	1597	1.703	53	Bridging bidentate

citrates through both bidentate and unidentate bindings. In addition, Table 5 shows that the intensity ratio of the symmetric mode at 1544 cm^{-1} to the asymmetric mode at 1597 cm^{-1} is greater than one, whereas the ratio of the other two symmetric modes are less than one. This shows that more bridging bidentate complexes were formed than unidentate and ionic complexes which suggests that the bridging bidentate complex is more favorable in stabilizing the nanoparticle core, probably due to the stronger bonding strength of the bidentate complex than the unidentate.

To compare the structural differences between the degraded and fresh nanoparticles, the Raman spectrum of an old batch (i.e. a few months old) of citrate-stabilized nanoparticles stored in the dark at room temperature was obtained using a 6-cm-long strand of HC-PCF (Fig. 18). CV dye adsorption with this old batch of nanoparticles was not successful and no SERS or Raman signal of the CV dye was obtained. The Raman modes at 1386 and 1454 cm^{-1} are assigned to the symmetric stretches of the carboxylates. Although the water mode at ~1652 cm^{-1} is strong, the carboxylate stretching modes at 1553 cm^{-1} and 1597 cm^{-1} were determined through fitting three Gaussian functions to the broad peak at ~1600 cm^{-1}. The Raman mode at 1553 cm^{-1} is assigned to the symmetric stretch while the 1597 cm^{-1} is assigned to the asymmetric stretch of the carboxylates.

Table 6 shows the carboxylate–metal complexes determined from the carboxylate stretching modes. The same three complexes were found in the degraded nanoparticle solution. However, the intensity ratio of the unidentate and ionic complexes is greater than one, in comparison to that observed in the freshly prepared nanoparticles. Furthermore, the ratio of the bidentate complexes is also reduced to less than one. This suggests that some of the bidentate complexes in the nanoparticle solution were changed to unidentate complexes, ionic complexes, and possibly detached from the gold core. Due to the lost of surface enhancement from the gold nanoparticles, free flowing citrates could not be

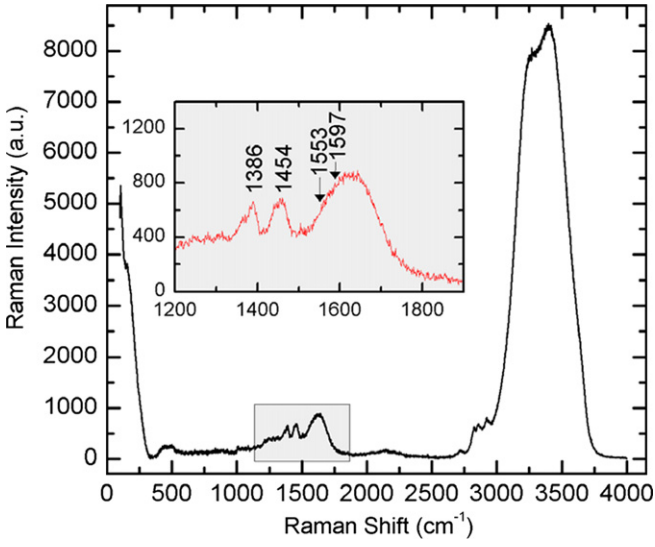

Fig. 18. Raman spectrum of citrate-stabilized gold nanoparticles stored for a few months. Inset: enlarge spectrum showing carboxylate stretching modes of citrate.

Table 6
Wavenumber position of the symmetric and asymmetric stretching carboxylate modes of citrate, their intensity ratio to $v_{as}(COO^-)$, respective wavenumber differences and proposed complexes for a six-month old batch of citrate-stabilized nanoparticles.

v_s(COO)	v_{as}(COO)	Intensity ratio of v_s(COO) to v_{as}(COO)	Wavenumber separation between v_s(COO) and v_{as}(COO) (cm^{-1})	Proposed structure
1386	1597	1.157	211	Unidentate
1454	1597	1.209	143	Ionic
1553	1597	0.658	44	Bridging bidentate

detected for comparison. Nevertheless, the reduction of bidentate complexes suggests that stabilization of the gold cores was weakened through long storage periods at room temperature. Furthermore, the loss of citrate anions might have reduced the adsorption strength of the Raman dye, as well as the phospholipid coating in the case of the phospholipid nanoparticles system, through diminished electrostatic interactions.

In addition to characterizing the structure of the gold nanoparticle probe, the power stability of the successfully synthesized probe is further evaluated using Raman spectroscopy with HC-PCF. Carbonization of the gold nanoparticle probe was observed at high power density which resulted in the detachement of the Raman dye and subsequently destroyed the SERS signal. The cause of carbonization was found to be rooted in the thermal denaturation of citrates on the gold nanoparticle surface. Damage threshold of the probe was further determined.

Citrate-stabilized gold nanoparticles purchased from Ted Pella Inc. were adsorbed with CV and coated with phospholipids. Then the nanoparticles were selectively filled into the central air core of a ~5 cm long HC-PCF (HC-1060 from NKT Photonics) for Raman measurements. Fig. 2 illustrates the setup for Raman measurements using HC-PCF. Raman spectra were taken at 0.17, 1.7, 4.3, 8.5 and 17 mW starting with the lowest power level. Spectra were taken continuously at each power until the spectrum was stabilized for two spectra. The samples were laser-exposed for 30 s for each measurement. The effective mode area in the PCF was estimated to be 34.13 μM^2.

For Raman active phospholipid gold nanoparticles with power density $< 49.8\ \mu W/\mu m^2$ (Fig. 19a and b), strong Raman modes of CV adsorbed on the gold nanoparticles were observed. With increasing exposure times at each laser power, CV modes did not shift nor became undetectable. This shows that CV structure remained stable upon exposure of the pump laser. However, the intensity counts of all the CV modes in the stabilized spectra (after 210–270 s of laser exposure) dropped to about 50–60% of the mode intensities of the first spectrum at each power. This suggests that prolonged laser exposure could have caused minor detachments of the CV molecules that were weakly adsorbed onto the gold nanoparticles. This minor detachment could be possibly caused by the increased local temperature arising from the clustering and heating of the gold nanoparticles, or due to photo-decomposition of the CV that may occur from absorption of the 633 nm laser line.

At 126 $\mu W/\mu m^2$ (Fig. 19c), the intensity of the CV modes reduced further; the spectral region between 1000 and 1760 cm^{-1} also broadened and transformed into two broad peaks around 1377 and 1583 cm^{-1} in the first spectrum. At maximum power density, 498 $\mu W/\mu m^2$ (Fig. 19d), the spectrum further converged into two broad peaks, at 1353 and

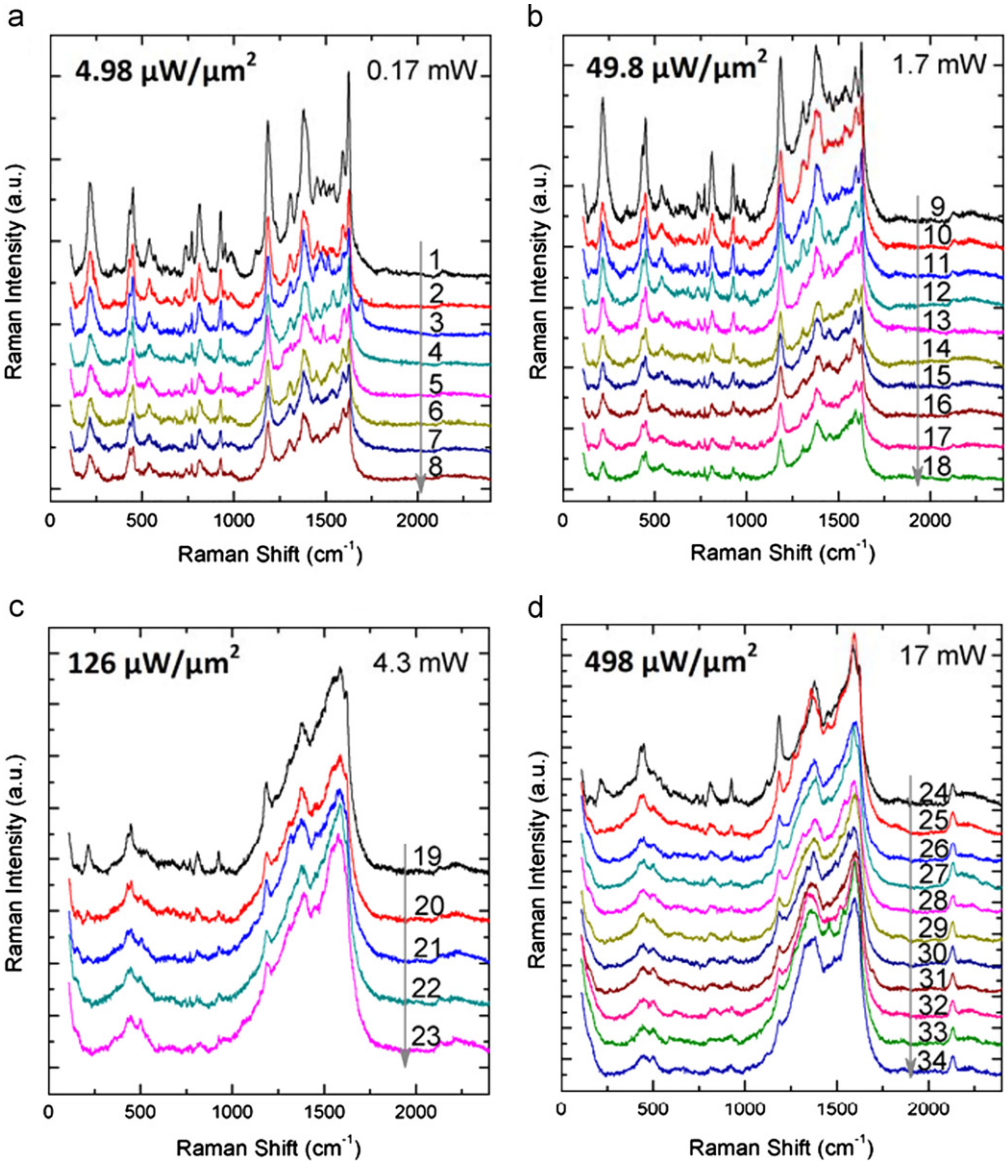

Fig. 19. Raman spectra of CV adsorbed gold nanoparticles with increasing power from 0.17 mW to (a) 1.7 mW (b), 4.3 mW (c), and 17 mW (d).

1594 cm^{-1}. The position and broadness of two peaks at 1353 and 1583 cm^{-1} are similar to those reported for carbon related structures such as amorphous carbon film [127] and graphite [128]. The mode at ~1353 cm^{-1} is referred to as the *D* peak (*D* for disordered) in which the feature correlates to the bond angle disorder between the carbon atoms. A highly disordered carbon structure, such as benzene clusters, contributes to an intense D peak [127]. The mode at ~1594 cm^{-1} is referred to as the G peak (G for graphite) as it is

correlated to graphite-like structures [127]. The origin of the carbon structures is not clear, but may be due to two sources in the nanoparticles — CV and citrate-stabilized gold nanoparticles. Raman spectra obtained from CV molecules did not exhibit any similar carbon-related peaks however.

For citrate-stabilized gold nanoparticles, similar to the phospholipid gold nanoparticles, no carbon modes were observed from citrate-stabilized gold nanoparticles at a power density $< 49.8\ \mu W/\mu m^2$ (Fig. 20a and b). However, at $126\ \mu W/\mu m^2$ (Fig. 20c), the spectrum converged into two peaks at 1353 (D peak) and 1576 cm^{-1} (G peak) similar to the two observed from the phospholipid gold nanoparticles. This pair of carbon peaks indicates that carbon structures were formed in the two nanoparticle systems: possibly upon thermal denaturation of citrates with a power density as low as $126\ \mu W/\mu m^2$ at 633 nm.

Our results suggest that some or all citrate molecules might still be left on the gold surface as similar changes of the Raman modes were observed in both the phospholipid

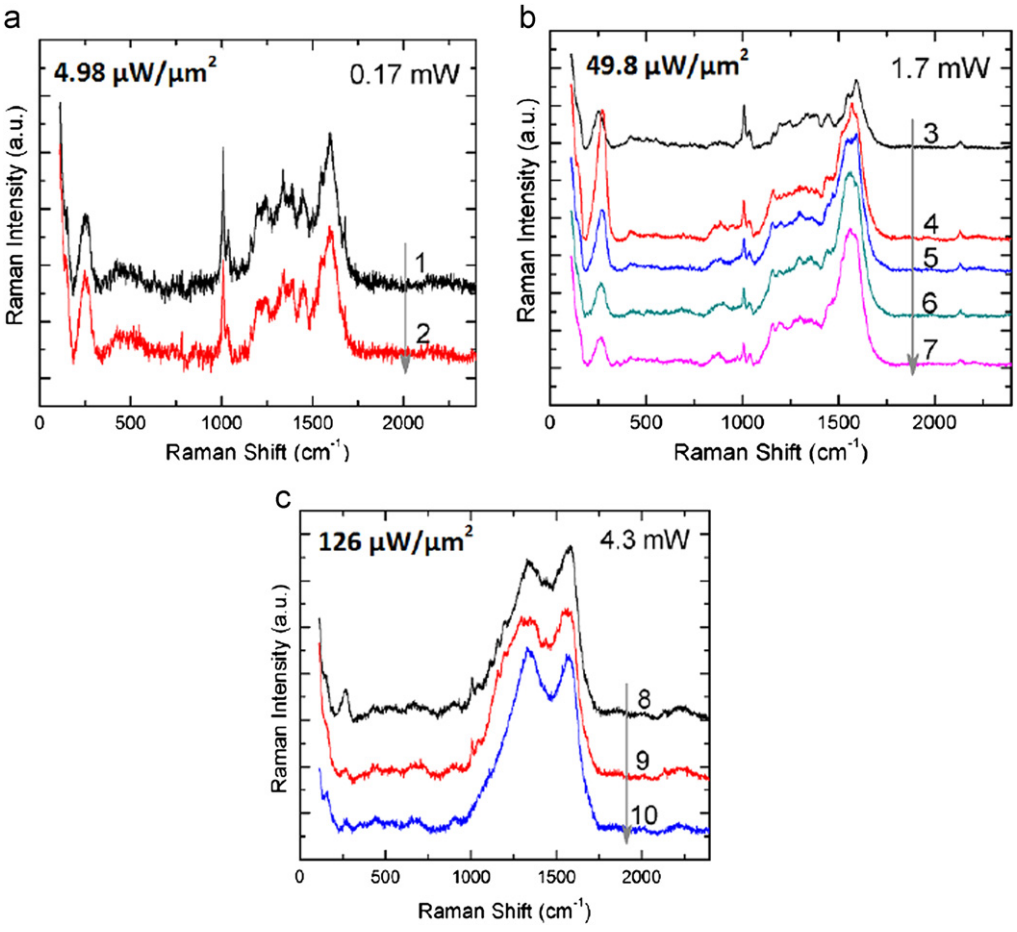

Fig. 20. Raman spectra of citrate-stabilized gold nanoparticles with increasing power from 0.17 mW to (a) 1.7 mW (b), 4.3 mW (c), and 8.5 mW (d).

gold nanoparticles and the citrate-stabilized nanoparticles. This further suggests that the use of Raman spectroscopy with HC-PCF might be a useful tool for determining the presence of citrates left on the Raman probe during and after synthesis.

4. Characterizing biological molecules

Raman spectroscopy is routinely used to identify and distinguish between different biological macromolecules. In conventional Raman spectroscopy (i.e. without the integration of optofluidic platforms or SERS enhancements), relatively large laser powers are typically employed to obtain a spectrum with high signal-to-background ratio [129–132]. However, these high laser powers may cause thermally induced destruction of the secondary or tertiary structures adopted by these macromolecules. With the use of a cover slide or a cuvette for Raman measurements in the conventional scheme, micro-liters to milli-liters of solution volumes are also required.

With the novel optofluidic technology described in this work, we can effectively obtain a high signal-to-noise and signal-to-background spectrum while maintaining the integrity of the biological molecules. This is achieved through an increased interaction length and improved collection efficiency of the Raman scattering signal provided by the optofluidic platform. The increased interaction length enables the pump laser to interact strongly with substances filled throughout the entire fiber length to generate Raman scattering signals while the increased collection efficiency improves the delivery of the generated Raman signal to the detector. These improvements significantly increase the sensitivity of the Raman spectroscopy technique, enabling weakly scattering biological samples to be resolved. Furthermore, the increased sensitivity enables a much lower pump power and sample volume (i.e. on the order of nano-liters) to be used to detect Raman scattering from biological samples. With a reduced pump power, the biological samples being measured are not exposed to temperature changes and therefore retain their native solution states at a particular temperature. In this section, we will discuss how optofluidic technologies have enabled the identification and detection of novel DNA conformations, and cancers in their early stage at their most native state.

4.1. DNA

Despite having only four building blocks, DNA can assume a plethora of conformations. Their structural variations not only stem from DNA sequential arrangements; environmental conditions such as pH, ionic strength, and humidity play crucial roles in determining the final structure of any oligodeoxynucleotide (ODN). An example of the structural diversity exhibited by nucleic acids is a group of four-stranded structures called G-quadruplexes. These structures arise from the stacking of at least two square planar arrangements of four guanine bases linked together by Hoogsteen hydrogen bonds termed G-quartets [133] (Fig. 21).

G-quadruplexes arise from DNA (or RNA) sequences that are rich in guanine bases and are dependent on the presence of monovalent cations that coordinate the O6 carbonyls from the guanines partaking in G-quartet formation. Such sequences are thought to be present in ~370,000 regions across our genome – suggesting a potential biological role [134,135].

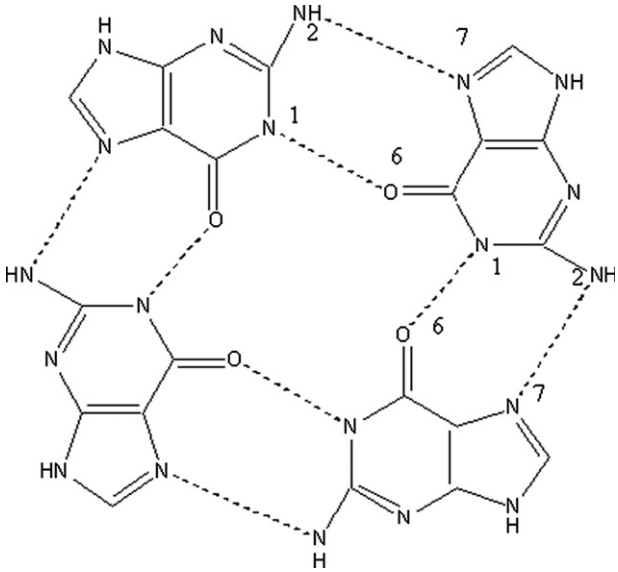

Fig. 21. Four guanine residues participating in Hoogsteen hydrogen bonds to form a G-quartet.

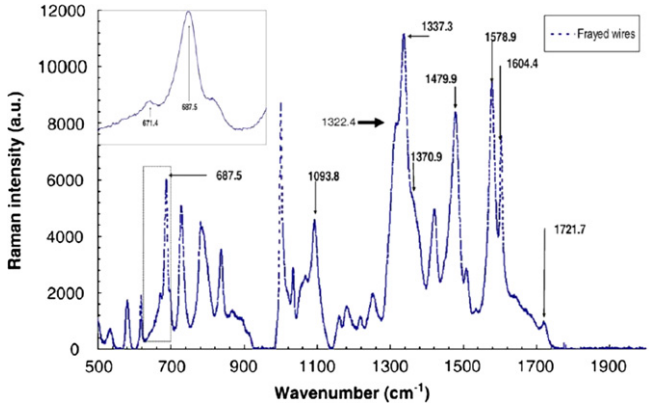

Fig. 22. Raman spectrum of 2 mM of d(A15G15) in 10 mM Tris–HCl (pH 7.5) and 100 mM KCl.

When long runs of guanine residues are present at terminal positions (i.e. 5′ or 3′) in an ODN, a set of superstructures spontaneously arise [136]. Such structures are termed DNA frayed wires. DNA frayed wires exhibit extreme thermostability, resistivity to chemical denaturants, and to nuclease digestion [137,138]. Based on methylation protection results, it was initially assumed that DNA frayed wires were distinct from G-quadruplexes in that N7 hydrogen bonding is not involved in stabilizing these structures [136,139]. However, once the Raman modes of a solution of d($A_{15}G_{15}$), a DNA frayed wire-forming sequence, were collected using photonic crystal fibers (PCF), it became evident that Hoogsteen hydrogen bond networks were present; hence, the DNA frayed wire structure is based

on the G-quartet motif [55] (Fig. 22). These are N7 hydrogen bonding (1479 cm^{-1}), O6 carbonyl coordination (1721.7 cm^{-1}), N1 hydrogen bonding (1604.4 cm^{-1}), and the C2–NH_2 marker emanating from G-quadruplex structures [140–142].

In addition to confirming that DNA frayed wires are a set of G-quadruplex structures, this novel Raman platform elucidated a previously unknown species within DNA frayed wires. Based on data collected from circular dichroism (CD) and from a conventional Raman system, DNA frayed wires were considered to have all four strands aligned parallel to each other [143]. By using PCF-enhanced Raman spectroscopy, Raman modes that arise from *syn* glycosidic conformations were observed [55]. Generally, guanine residues partaking in G-quartet formation assume *anti* glycosidic conformations in all-parallel structures; while those that are classified as antiparallel G-quadruplexes are composed of a combination of *anti* and *syn* glycosidic conformations [144]. Therefore the presence of two weak modes (671.4 cm^{-1} and 1322.4 cm^{-1}) that correspond to guanine *syn* conformations suggested that a small fraction of DNA frayed wires assume antiparallel conformations (Fig. 22 inset). In order to confirm these results, we employed a chemically modified oligonucleotide with the same sequence with the exception that the guanine residues were brominated at the eighth position. Guanine bases that bear this modification tend to assume a *syn* conformation due to steric constraints [145]. The CD spectrum of $d(A_{15}^{8\text{-Br}}G_{15})$ provided evidence of what appears to be a characteristic signature of antiparallel G-quadruplexes [55]. Additionally, once resolved electrophoretically, $d(A_{15}^{8\text{-Br}}G_{15})$ provided evidence of a dimeric species while all other DNA frayed wire bands were difficult to observe [55]. From the results obtained by PCF-enhanced Raman spectroscopy, it was revealed that DNA frayed wires were in fact G-quadruplexes and that the vast majority of the DNA superstructures were parallel-stranded with a fraction of antiparallel dimeric species.

Another G-quadruplex sequence that was examined using the PCF-enhanced Raman platform is the human telomeric (*H*-Tel) sequence. This sequence, and in particular the four-repeat d(5′-A$(GGGTTA)_3$GGG-3′), has been studied extensively due to the variety of structures it adopts. In the presence of sodium, the Nuclear Magnetic Resonance (NMR)-resolved solution structure is one of an antiparallel monomolecular G-quadruplex [146]. However, in the presence of potassium the crystal structure was that of a monomolecular parallel-stranded G-quadruplex [147]. Furthermore, the appending of either the 5′ or the 3′ end of this sequence revealed yet another set of monomolecular structures in the presence of potassium cations. The prevalent structure in these cases is termed the "3+1" configuration where three strands are aligned in parallel to each other, while the fourth lies in the opposite direction [148–152]. These structures have an additional feature whereby the uncomplexed bases at either the 5′ or 3′ end form capping structures (30 and 34). There are several reports on the structures that the four-repeat of *H*-Tel, along with its derivatives, adopt in response to changes in pH, cation species, molecular crowding, etc. However, there is a modest number of reports on how these oligonucleotides respond to changes in their concentration with the exception of the work of Renčiuk et al. [153].

The biophysical methods employed to study biological molecules are diverse. The analyte concentrations required for them are similarly diverse. For example, NMR and non-resonant Raman spectroscopies require millimolar concentrations, whereas CD and UV absorption methodologies require micromolar concentrations of DNA or proteins. As such, we chose to study *H*-Tel and two of its variants, d(5′–**AAA**GGGTTTAGGGTTAGGGTTAGGG**AA**-3′) and d(5′–**TTA**GGGTTAGGGTTAGGGTTAGGG**TT**-3′), hybrid 1 (Hyb-1) and hybrid

2(Hyb-2), respectively, at concentration values that cover the micromolar to the millimolar range (bold letters highlight the sequence deviations from *H*-Tel).

In the presence of sodium cations, the CD spectra from 20 μM to 2 mM *H*-Tel are drastically different, with the latter changing gradually as a function of time. The CD spectrum of the former resembled that of the established antiparallel conformation reported previously while the latter appeared to be similar to parallel stranded conformations. Subsequently, the changes of the CD signal at 258 nm were monitored as a function of time with varying concentrations of *H*-Tel (3–7 mM). The relaxation times observed were concentration-dependent suggesting that the changes occurring are due to aggregation. Furthermore, the relaxations were fit bi-exponentially, except the 7 mM sample which was best fit monoexponentially. Interestingly, both Hyb-1 and Hyb-2 samples did not display the same behavior as *H*-Tel. Instead, both oligonucleotides

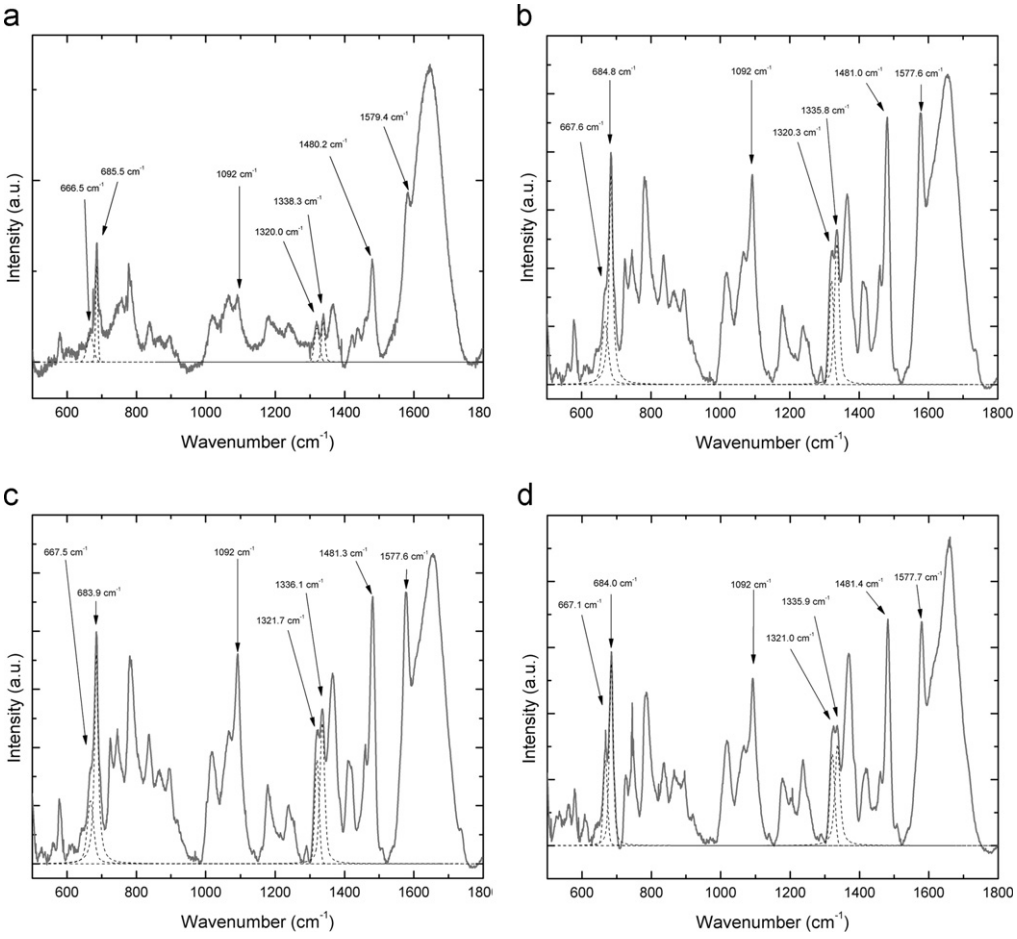

Fig. 23. Raman spectra of d(TG_4T) in 10 mM Tris–HCl and 100 mM KCl (a); *H*-Tel in Tris–HCl and 100 mM NaCl (b); Hyb-1 in 10 mM Tris–HCl and 100 mM KCl (c); Hyb-2 in 10 mM Tris–HCl and 100 mM KCl (d). All samples contained 2 mM of ODN and incubated for 48 h at 25 °C.

provided the equivalent CD spectra at high (mM) and low (μM) strand concentrations. However, only when the cation concentration (K^+) increased 10-fold did Hyb-1 and Hyb-2 behave similar to *H*-Tel at millimolar strand concentrations.

To further characterize the structure(s) forming at high oligonucleotide concentrations, PCF-enhanced Raman spectroscopy was employed. Fig. 23 displays the Raman spectra of d(TG_4T), *H*-Tel, Hyb-1, and Hyb-2 after an incubation period of 48 h. The d(TG_4T) oligonucleotide was chosen as a reference since it readily forms a parallel stranded tetramolecular G-quadruplex with the guanines partaking in G-quartets assuming an *anti* glycosidic conformation. In this case, this oligonucleotide provided an intense 1480.2 cm^{-1} indicating the presence G-quartets [142]. Additionally, the *anti* guanine band at 685.5 cm^{-1} was much more intense than the band corresponding to the *syn* conformation at 670 cm^{-1}. The Raman spectrum of *H*-Tel also provided evidence of G-quadruplex formation (1481 cm^{-1}) along with a clear *anti* marker (686.6 cm^{-1}) with a small *syn* mode (667.6 cm^{-1}). Similarly, Hyb-1 and Hyb-2 displayed the characteristic G-quadruplex marker at 1481 cm^{-1} with the *anti* band at 684 cm^{-1} and a shouldering *syn* band at 667 cm^{-1}. Fig. 24 compares the guanine *anti*(~685 and 1335 cm^{-1}) and *syn*(~670 and 1325 cm^{-1}) Raman modes of *H*-Tel, Hyb-1, and Hyb-2 at two time points. The first ($t=0$) corresponds to the time when the aqueous buffer (including 100 mM of either Na^+ or K^+) was mixed with the DNA, and the second is after a 48-hour incubation period at 25 °C. From this figure it is evident that G-quadruplexes are present in all cases and at both time points. Furthermore, *H*-Tel was the only sequence that the *anti*:*syn* Raman mode ratios were changing as a function of time; where the *syn* mode was slowly being depleted while that of the *anti* mode was increasing.

From the data presented above, *H*-Tel appears to be forming a G-quadruplex aggregate with more *anti* guanines than *syn* conformations. This suggests that these aggregates possibly have parallel-stranded topologies. Finally, Hyb-1 and Hyb-2 sequences did not display the same time-dependent transition as *H*-Tel did. A possible explanation to this observation is the fact that these sequences, once folded, contain capping structures that further stabilize the monomolecular conformations over the aggregated species.

4.2. Early stage cancer detection

The ability of detecting human cancers at an early stage is critical for increasing the effectiveness of cancer treatment and improving the survival rate of the patients. Detecting cancer at an early stage remained very challenging as the number of tumor cells present is very low. An ultra-sensitive technique would be required to detect, distinguish and identify cancer cells from normal ones. One way to detect cancer cells is through the unique markers on the cells themselves [154–157]. Specific tumor antigens and receptors that are typically overexpressed on the surface of cells can be used to identify and target these cancer cells. Antigens and receptors are characterized by their unique capability of binding specifically to antibodies, or anti-receptor antibody, respectively. As an example, the epidermal growth factor receptor (EGFR) is overexpressed in the majority of lung tumors [158–160].The introduction of an EGFR antibody will allow the antibody to bind specifically to the EGFR which is an effective way to selectively target the lung tumor cells.

Recently, a novel way of detecting cancer cells with Raman spectroscopy using cancer markers has been demonstrated [92,161–163]. This technique was achieved by synthesizing nanometer-sized probes composed of metallic nanoparticles functionalized with both

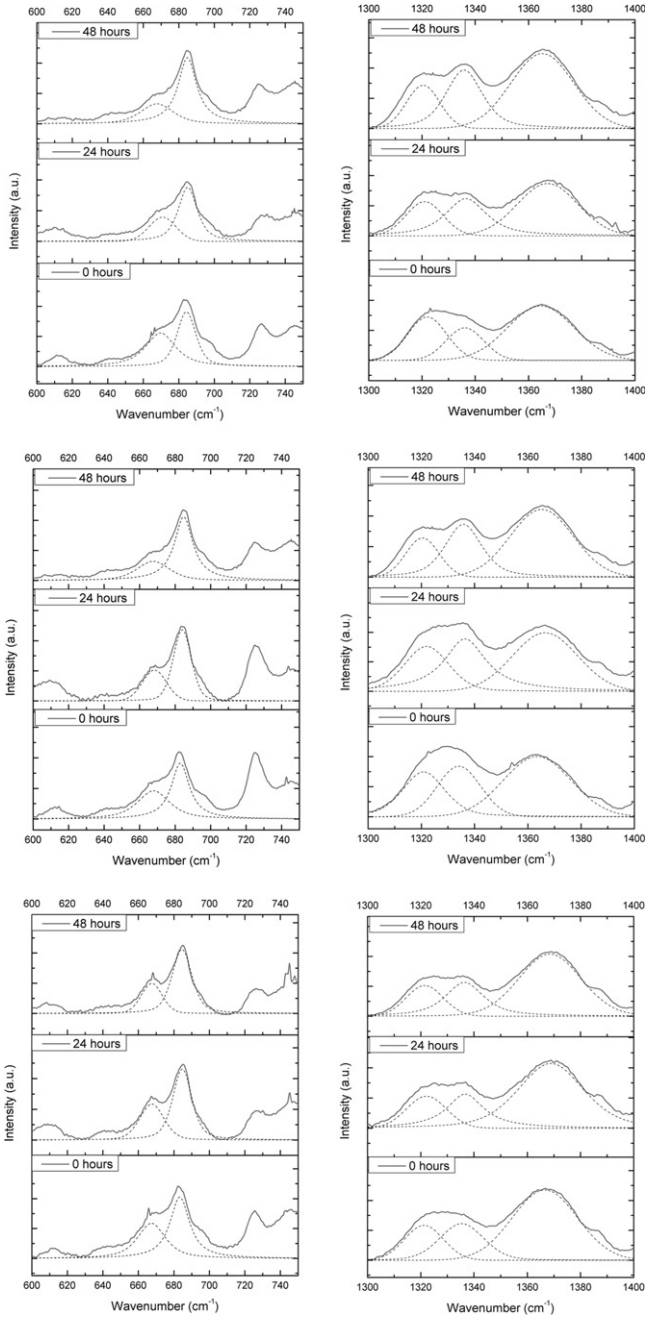

Fig. 24. Monitoring the changes of the *anti* and *syn* Raman modes in the spectral regions of 600–740 cm^{-1} (left column) and 1300–1400 cm^{-1} (right column) of *H*-Tel (top); Hyb-1 (middle); Hyb-2 (bottom). All samples contained 2 mM of ODNs dissolved in 10 mM Tris–HCl, pH 7.5, and either 100 mM NaCl (*H*-Tel) or 100 mM KCl (Hyb-1 and Hyb-2).

Raman reporters and antibodies. The antibodies are chosen so that they bind with receptors overexpressed on the targeted cancer cell. When the nanoparticle probe attaches to the cancer cell, Raman scattering signals from the reporter would be enhanced as the nanoparticle probes aggregate together around the cell surface that contains the targeted receptors. This gives a strong detectable Raman scattering signal indicating that a particular type of cancer cell is present. In the case where cancer cells are not present, or that a different type of cancer cells are present, that do not overexpress that particular targeted receptor, the nanoparticle probes will distribute randomly in the solution. Thus, no or very limited electromagnetic enhancement from the nanoparticles will be achieved and no Raman modes or very weak Raman modes of the Raman reporter will be detected. Traditionally, fluorescent particles such as QDs were used instead of Raman probes. However, fluorescent particles are limited by their large bandwidth (FWHM =40–60 nm) which is about 20–30 times wider than that of the Raman modes, limiting its capability for multiplexing different reporters together. These particles are also susceptible to photobleaching and quenching under high laser powers and long laser exposure times; while Raman probes would not [164]. Moreover, the use of routine histology stains for cell morphology assessment can interfere with fluorescent labels in optical imaging [161]. Therefore, Raman probes are a more suitable targeting and reporting technique with greater multiplexing capability than QDs for cancer detection.

Detection of cancer cells from different parts of the human body has been demonstrated using various Raman probes. These cancers include oral cancer [165], human head-and-neck cancer [92], kidney cancer [166], chronic lymphocytic leukemia [161], colon cancer [166], and circulating tumor cells in the blood [167]. Raman probes involved in these experiments include those composed of a gold core functionalized with a Raman reporter, such as MGITC, and conjugated with antibodies, such as the anti-EGFR antibody that target antigens and receptors overexpressed on cancer cells [116]. In contrast, Liu et al. have demonstrated the use of carbon nanotubes as the Raman probe [168]. Carbon nanotube has a G band peak at 1530 cm^{-1} without the attachment of a Raman reporter. With chemical vapor deposition, the position of the G band peak can be shifted though using different growth gas ratios of the C13 methane and the C12 methane. This enabled five carbon nanotube probes to be multiplexed to target five different cancer cells simultaneously through Raman imaging without any spectroscopic interference.

Sha et al. [169] and Gong et al. [170] have also demonstrated the use of two separate nanoparticles for targeting and reporting in an immunoassay. Raman probes synthesized with antibody-conjugated silica coated with silver or gold nanoparticles were used to report through a Raman reporter while an antibody modified magnetic nanoparticle was used to target and capture the antigen. This technique reduced the overall detection time through avoiding the complicated pre-treatment and watching steps in conventional Raman immunoassays.

Qian et al. have also demonstrated, for the first time, the use of pegylated gold Raman probes for in vivo targeting and detection of human head-and-neck carcinoma cells in a live animal model [92]. Malachite green isothiocyanate (MGITC) was adsorbed onto the surface of the 60 nm gold nanoparticles to use as a Raman reporter. ScFv antibody, a ligand that binds to the EGFR with high specificity and affinity, was then conjugated onto the nanoparticle probe after coating it with a layer of PEG polymers (targeted nanoparticles). Nanoparticles coated with a PEG polymer layer but not conjugated with ScFv antibodies were used as a negative control (non-targeted nanoparticles).

The nanoparticle probes were injected systemically into two nude mice (through tail veins) bearing a human head-and-neck tumor (Tu686). SERS spectra obtained 5 h after using 785 nm laser beam showed strong SERS signals from MGTIC from the targeted nanoparticles at the tumor site. Similar weak SERS signals were observed from the non-targeted nanoparticles and the non-specific liver site; indicating that the ScFv-conjugated gold nanoparticles were able to target EGFR-positive tumors in vivo.

Early stage cancer detection will be of great clinical significance as it would provide an opportunity to commence relevant treatment relatively early. Recently, Dinish et al. have demonstrated the detection of EGFR positive human epithelial carcinoma cells using only ~10 nL of a sample volume through the use of HC-PCF [171]. Cell lysate solutions from EGFR positive human epithelial carcinoma cells (A431) and the control, EGFR negative human breast carcinoma cells (MCF-7) were first filled to the core of the two separate 8-cm-long HC-PCF (HC 800-01, NKT Photonics) for protein binding. Then, anti-EGFR conjugated gold nanoparticles with adsorbed MGITC were immobilized into the PCF core for Raman detection. As the SERS tags only bind to the fiber with EGFR bound to the fiber, the SERS spectrum of the Raman dye, MGITC, was obtained from the fiber with cancer proteins from A431 (i.e. indicating that EGFR positive cancer cells were present); while no SERS signals were obtained from samples containing the MCF-7 cancer protein. A power of 0.6 mW of a 633 nm laser was used in this experiment, and the proteins were at a concentration that was in the range of about ng/mL–μg/mL. The high sensitivity of this technique is attributed to the increased light–matter interaction between the pump laser light and the Raman reporter, as well as the improved collection efficiency with the selectively filled HC-PCF.

One limitation of this technique is that the binding process between the protein and the SERS tag has to take place within the central core of the PCF. Due to the small core size of the PCF, this technique is limited to small biological matter such as proteins and DNA. Large biological matter such as cancer cells, with size typically on the order of 10 μM, would be difficult to be immobilized directly into the central core of PCF that are typically smaller than 20 μM in diameter. Moreover, immobilization of large whole cells into the PCF would make binding interaction difficult as it would leave very little space for the nanoparticle probes to be filled into the fiber core. Thus, extraction of cell lysates is required, which complicates the preparation process.

5. Combining surface enhanced Raman spectroscopy with optofluidic devices

When optofluidic devices are combined with SERS, Raman analysis with sensitivity higher than that of each technique alone could potentially be achieved. This is ideal for identifying analytes with small Raman cross-sections, as well as interactions between analytes, in which extremely high sensitivity is required to obtain a strong and clear Raman spectrum. Since detailed analysis of the Raman modes is typically not required in material identification; changes in Raman modes' positions, FWHMs, and relative intensities, due to the addition of metallic nanostructures, are not of a concern.

Through combining SERS with optofluidic devices, the detected SERS signal could be further enhanced through the increased interaction length and collection efficiency. In the confined space inside the optofluidic channel, more metallic nanoparticles could be excited by the pump laser and interact with the analyte. Therefore, SERS signals obtained from optofluidic devices could be greater than that in conventional SERS measurements.

The combined technique reduces the limit of detection in SERS measurements; thus, enabling the detection of solutions at concentrations that are not detectable with either technique alone. In addition, metallic nanostructures could be used as probes to selectively enhance Raman modes of only one or several specific types of analytes. This reduces mode interferences in the Raman spectrum and further reduces the limit of detection. Furthermore, optofluidic devices significantly reduce the sample volume required to as low as nano-liters. Thus, the amount of metallic nanostructures required for enhancement is also reduced considerably. In this section, we will review three different ways of integrating metallic nanostructures into optofluidic devices for ultra-sensitive SERS measurements.

5.1. Mixing metal nanomaterials with analytes

The simplest method to integrate metallic nanoparticles with optofluidic devices for SERS measurements is to mix metallic nanoparticles together with the analyte, then fill the mixed solution into the optofluidic device. Upon excitation of the metallic nanoparticles in the mixed solution with the pump laser propagating in the PCF, strong SERS signals can be generated and collected back by the PCF to the detector.

Zhang et al. have demonstrated enhancements in the retrieved SERS signal from tryptophan spectra using the described technique [172]. SERS substrates were mixed with tryptophan solutions at a concentration range of $\sim 10^{-4}$–10^{-5} M and the resulting mixed solution was selectively filled into the core of a 10-cm-long HC-PCF by dipping the HC-PCF into the mixed solution for 5 s (i.e. filled the central core of the PCF by ~1 cm). SERS measurements were obtained with a 785 nm laser at 3 mW with a scanning period of 20 s. In comparison with the SERS signal obtained from a 100 μL sample of the same solution dried on a crystal substrate, the normalized SERS signal was ~100 higher when it was obtained from the mixed solution in HC-PCF. Furthermore, with selectively filled HC-PCF, R6G, human insulin, and tryptophan were detected at concentrations of $\sim 10^{-4}$–10^{-5} M while only R6G was detected with non-selectively filled HC-PCF at such low concentrations. This demonstrated that HC-PCF can enhance the retrieved SERS signal beyond that of SERS alone. The enhancement was achieved through strong confinement of the analyte, SERS substrate, and the pump laser light in the same central core of the HC-PCF, which thereby increased the light–analyte interactions, as well as the improved collection efficiency of the SERS signal generated in the HC-PCF.

Han et al. also compared the retrieved SERS signal of thiocyanate anions (NaSCN), at a concentration of 1.7×10^{-7} M, using a conventional Raman technique with a glass vial and that with HC-PCF selectively filled with the mixed SERS particle-analyte solution [78]. SERS measurement obtained using selectively filled HC-PCF showed a pronounced SCN^- stretching vibrational mode at 2100 cm^{-1} in addition to the water bands at 3400 cm^{-1}. Without using HC-PCF as the medium for light–matter interactions, SERS measurement from the glass vial showed only the water bands and was unable to detect the SCN^- mode at the same concentration.

Yang et al. have further compared the enhancement factors between SERS and Raman spectroscopy using liquid filled HC-PCF [70]. Using R6G as a reference, 25 nm silver nanoparticles for SERS enhancements, and 2 mm long HC-PCF as the interaction medium, the enhancement factors of HC-PCF-assisted Raman spectroscopy relative to direct sampling were found to be 97 in SERS and 61 in Raman spectroscopy. Simulation showed that HC-PCF significantly increased the transmission range and provided strong

light confinement in the PCF core and cladding when all channels of a HC-PCF were filled with water. This resulted in an increased number of particles involved in SERS; thus, a greater enhancement was achieved. It is important to note that these enhancement factors were not normalized in relation to the interaction volume. Therefore, the actual enhancement factors should be higher after they are normalized with the interaction volume being considered since the HC-PCF setup required less sample volumes than that in direct sampling.

Instead of using optofluidic fibers, Measor et al. have demonstrated SERS detections with integrated LCW using interconnected solid- and liquid-core antiresonant reflecting optical waveguides (ARROWs) [173]. Using a 633 nm excitation, SERS spectra of R6G solutions mixed with 20 nm silver nanoparticles were detected at concentrations as low as 30 nm with an excitation volume of 44 pL. This concentration limit was said to be comparable to the reported 10 nm limit in a silica capillary with SERS-active silver nanoparticles [174]. However, the analyte and silver nanoparticles between the two published papers were different; therefore, a fair comparison could not be made.

Metallic nanoparticles often aggregate in the presence of the analyte due to changes in the sample environment (i.e. pH values). Due to the small size of the central core and cladding holes in PCFs, particle aggregation in the sample could block the entrance to the PCF and limit the length of PCF in which the solution can have access to with capillary action; thus, limiting the benefit of long interaction length of the optofluidic fiber. To fill the mixed solution through the entire length of the PCF, Xie et al. demonstrated a simple technique to inject the mixed solution into the PCF using a modified syringe setup [175]. In their report, a 4-mercaptobenzoic acid (4-MBA) aqueous solution (0.01 mM, 200 μL) mixed with 100 μL of Ag colloid were filled into two 10-cm-long PCFs – one through capillary action, which filled only ~1 cm of the PCF before filling was obstructed, and the other through the simple pressure setup with the modified syringe, which filled the mixed solution throughout the entire fiber length. The resulting SERS spectra obtained from the two PCFs showed that the 4-MBA Raman modes obtained from the PCF utilizing the pressure setup was three times stronger than that obtained from the PCF filled via capillary action as a result of benefiting from the full length of the HC-PCF.

5.2. *Adsorbing metal nanomaterials with analytes*

A more controllable and reproducible method to maximize SERS enhancement is to conjugate, or adsorb, analytes onto the surface of the metallic nanostructures by surface modification. In the analyte–metal mixing technique described previously in Section 5.1, interactions between the analyte and the metal are random and dynamic as they are driven mainly by fluidic flow and random movements of the particles causing uncontrollable fluctuations in SERS enhancements. By conjugating or adsorbing analytes onto the surface of the metallic nanostructures, the analytes can be fixed at a near distance from the metal which enables the SERS enhancement to be maximized and the resulting SERS spectrum to be stabilized. Furthermore, the adsorption process can reduce surface charges of the analyte and the nanostructure which would minimize Raman mode interferences introduced from interactions with the sidewall of the optofluidic device. As a result, conjugation and adsorption can increase the detection sensitivity of the analyte further from merely mixing the analyte and the metallic nanostructure together.

Recently, we demonstrated 10-fold enhancements from the detected Raman spectrum, compared to conventional Raman spectroscopy, of the Congo Red dye by adsorbing it onto gold nanorods and detecting the Raman spectrum using HC-PCF [57]. In this work, the Congo Red dye molecules were adsorbed onto the surface of the cytotoxic cetyltrimethylammonium bromide (CTAB)-coated gold nanorods with an average length and width of 38.42 ± 2.69 and 8.75 ± 0.61 nm, respectively. The respective localized surface plasmon resonance wavelengths of the gold nanorods are centered at 510 and 773 nm. The concentration of the Congo Red solution was 3 μM. The Raman spectrum of the resulting solution was acquired with a 633 nm HeNe laser through direct sampling and by selective filling the solution into the core of a 7 cm long segment of HC-PCF (HC-1060 from NKT Photonics) with a core diameter of 9.5 μM.

Fig. 25 compares the acquired SERS spectra using gold nanorods, through direct sampling and with HC-PCF, with the Raman spectrum acquired from 564 μM of Congo Red alone. It is clearly shown that the Congo Red spectrum obtained from adsorbing it onto the gold nanorod and by selectively filling the solution into the core of the HC-PCF is significantly enhanced compared to that obtained from conventional Raman spectroscopy. Furthermore, by selectively filling the analyte adsorbed nanorod solution into core of HC-PCF, we demonstrated that the retrieved Raman signal is further enhanced compared to the stabilized and maximized SERS enhancement alone. The signal-to-noise of the spectrum was also improved considerably through the use of the HC-PCF platform. By using the Raman mode at 1167 cm^{-1} as a reference, the peak intensity of the SERS signals from using HC-PCF is increased by 10-fold compared to that of conventional Raman spectroscopy using a cuvette. By using the Au–Br mode at 178 cm^{-1} from the CTAB-coated nanorod as a reference, the limit of detection with gold nanorods was found to be improved by 100 times from 14.4 nm, by using a cuvette, to 0.14 nm with selectively filled HC-PCF (Fig. 26).

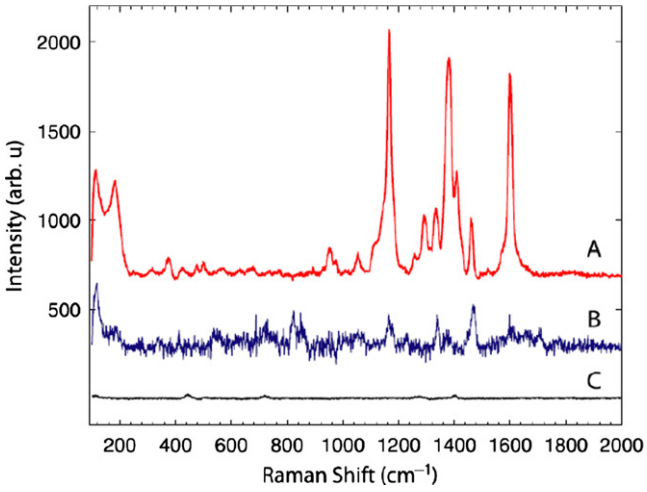

Fig. 25. SERS spectra of a 3 μM Congo Red solution acquired by core-filled HC-PCF technique (A) and direct sampling technique (B). Ordinary Raman spectrum of a 564 μM Congo Red solution (C). Spectra are shifted vertically for clarity.

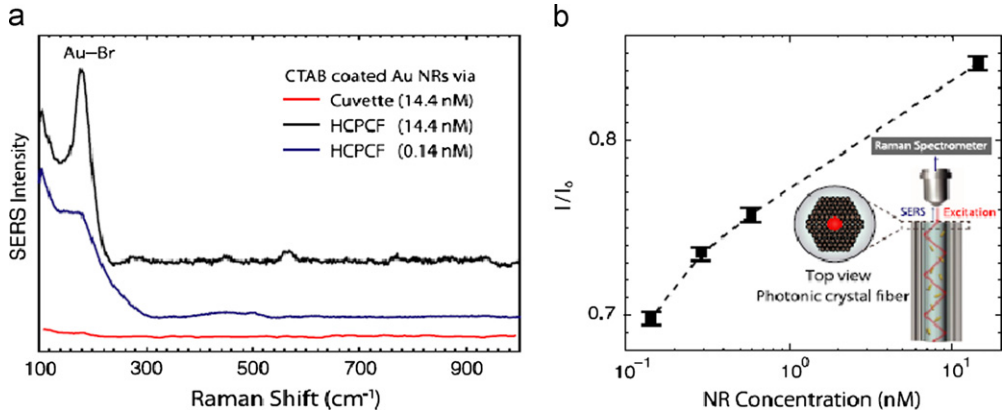

Fig. 26. (1) SERS spectra of CTAB-coated nanorods obtained with a cuvette and by selectively filling of nanorod solutions into the core of HC-PCF. The limit of detection was improved from direct sampling with a cuvette by 100 times with selectively filled PCF. (b) Normalized Au–Br mode intensity as a concentration of CTAB-coated nanorod. Mode intensity was normalized to that obtained using direct sampling with a cuvette.

With the 10-fold enhancement from combining the use of SERS, with analytes conjugated to metallic nanostructures, and HC-PCF, with the selective filling technique, we further demonstrated the capability of using Raman spectroscopy to observe the ligand exchange process in gold nanorods at very low concentrations. Ligand exchange is the process to exchange the agent stabilizing the nanostructure for the ligands. In this study, CTAB on the surface of the nanorod was replaced with α-methoxy-ω-mercaptopoly-(ethylene glycol) (SH-mPEG) (molecular weight 12,000 g/mol). This ligand exchange is typically required to minimize toxicity of the solution by replacing the cytotoxic CTAB molecules with a non-toxic compounds like SH-mPEG for use in the blood circulation system [176].

Fig. 27 shows the SERS spectra obtained during the SH-mPEG/CTAB exchange in aqueous solutions using HC-PCF. As the concentration of SH-mPEG increases, the intensities of CTAB Raman modes at 178, 1155, 1387, and 1512 cm^{-1} decrease. This indicates that the CTAB molecules on the surface of the nanorods are gradually being replaced by SH-mPEG polymers with increasing SH-mPEG concentration. In this exchange process, the concentration of the nanorods was maintained at 0.54 nm, a low concentration in which the Raman modes of CTAB could not be observed with the direct sampling technique. Through the large 10-fold enhancement, a complete exchange of CTAB by SH-mPEG was clearly observed.

5.3. Coating central core of hollow-core photonic crystal fibers with metallic nanomaterials

Another scheme to integrate metallic nanomaterials with HC-PCF for ultra-sensitive SERS measurements is to coat metallic nanostructures onto the inner sidewall of the HC-PCF's central core throughout the fiber length. By selectively filling the analyte of interest into the metallic-nanoparticle-functionalized central core of the HC-PCF, strong SERS enhancement can be achieved throughout the entire fiber length upon excitation of the immobilized metallic nanoparticles with a pump laser.

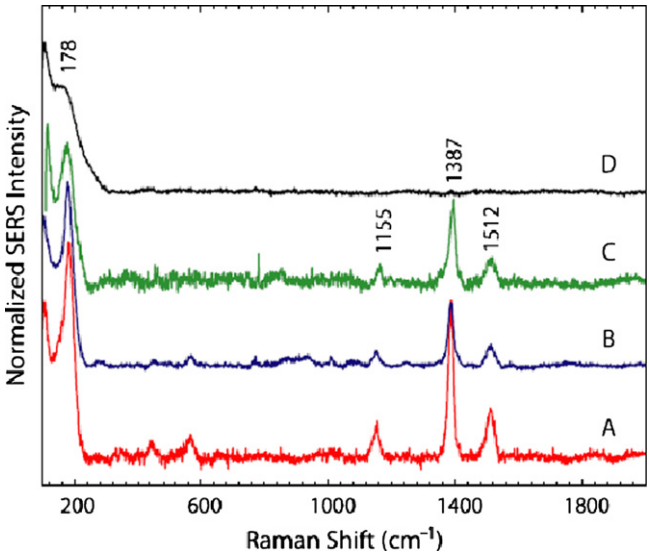

Fig. 27. Normalized SERS spectra of CTAB-coated nanorods with increasing SH-mPEG concentrations: (A) no PEG, (B) 20 μM of PEG, (C) 50 μM of PEG and (D) 100 μM of PEG. Spectra are vertically shifted for clarity.

One advantage of such technique is that the random motions of the colloidal nanoparticles are eliminated by having the metallic nanostructure immobilized onto the sidewall of the PCF core which would improve the reproducibility of the SERS signal. A greater control over the nanoparticle density and aggregation could also be controlled potentially to further improve the reproducibility of the SERS effect. However, fewer Raman scattering signals could be potentially produced compared to filling the PCF core with premixed analyte-SERS particle solution due to the weaker light intensity at the sidewall, where the nanoparticles are immobilized, rather than the center of the core. In fact, preserving the light guiding characteristics of the PCF after coating with the nanoparticles remains a challenge. Moreover, it is difficult to immobilize nanostructures onto the inner sidewall of the PCF core with controlled density coverage and throughout the entire fiber length due to the small core size (i.e. <20 μM in diameter) of the HC-PCF.

Recently, Han et al. reported for the first time SERS accumulated from 20-cm-long strands of full-length Ag-nanoparticle-functionalized PCFs [177]. HC-PCF was functionalized with Ag nanoparticles using a polyelectrolyte-mediated surface immobilization technique for noble nanoparticles. In this technique, polyallylamine hydrochloride (PAH) was filled into the central core of the HC-PCF for adsorption onto the inner sidewall to create anchoring sites for the Ag nanoparticles. This was followed by filling the PCF core with a Ag-nanoparticle (35 ± 5 nm) solution for immobilization. Both the PAH and Ag nanoparticle solutions were filled into the fiber core through maintaining a 200 psi pressure differential between the two ends of the HC-PCF, with the cladding holes sealed, in a custom-built pressure cell. By changing the pH values of PAH for adsorption, different density coverage of Ag nanoparticles can be controlled such that at higher pH values, PAH will enable a higher Ag nanoparticles density to be immobilized.

The performance of the Ag-nanoparticle functionalized HC-PCF was evaluated by filling R6G into the central core. With a 633 nm laser in a forward-scattering configuration,

Raman modes of R6G were observed at concentrations as low as 10^{-7} M using HC-PCF functionalized with Ag nanoparticles. Han et al. further stated that for planar substrates with the same Ag nanoparticle coverage density, no SERS could be observed at a higher R6G concentration of 10^{-5} M.

Raman spectra of R6G were also obtained at different fiber lengths (up to ~27 cm) and particle densities (0.2, 0.5 and 4 particles/μm^2). It was found that the benefit of SERS accumulation with prolonged length of a PCF was only observed at low Ag nanoparticle density (i.e. below 0.5 particle/μm^2). Using the Raman mode at 1351 cm^{-1} as a reference, it was found that the Raman intensity increased with increasing fiber length at nanoparticle densities below 0.5 particles/μm^2. This demonstrated a net accumulation of SERS signal along the PCF length. At higher nanoparticle densities, at and beyond 0.5 particles/μm^2, Raman intensities were found to decrease with increasing fiber length. This suggested that scattering and absorption losses of the pump laser and the Raman scattering signals began to dominate in the prolonged fiber. As a result, no overall gain in SERS signal with increased PCF length in the forward-scattering configuration was found.

Utilizing the same immobilization technique, Ag nanoparticles immobilized into the cladding air holes of the SC-PCF was also demonstrated and evaluated with R6G filled into the functionalized cladding holes. The obtained SERS signals were increasing with increased fiber length at 0.1 particles/μm^2, and decreasing with increased fiber length at 4 particles/μm^2 as observed in HC-PCF. However, strong interference from the silica Raman modes were observed with the SC-PCF due to overlaps of the pump laser light and the silica cladding walls as discussed in Section 2.2. Furthermore, lower Raman intensities of the R6G modes were obtained in SC-PCF compared to those obtained in HC-PCF under the same experimental conditions (i.e. PCF length, pump power, pump wavelength, particle density, and R6G concentration).

Oo et al. also immobilized Ag nanoparticles in SC-PCF using the same technique as Han et al. but instead used gelatin to create anchoring sites for Ag nanoparticles as opposed to PAH [65]. With 2 mg/mL gelatin solutions at pH 10, 1 particle/μm^2 density coverage of Ag nanoparticles was achieved and 2 μM of R6G was observed with a 633 nm laser at ~5 mW with acquisition times of 10 s in a forward-scattering configuration. Nevertheless, strong interferences of the silica Raman modes were also observed with the functionalized SC-PCF in this report.

In addition to coating the inner sidewalls of the central core in HC-PCF with metallic nanoparticles, Shi et al. further reported SERS spectra of R6G when a mixture of analytes and Ag nanoparticles were filled into a Ag-nanoparticle-functionalized core of HC-PCF [178]. This group filled a 5 ± 2 nm Ag nanoparticle solution into the central core of a HC-PCF, with its cladding holes sealed, using a syringe needle, and dried it for 20 min to immobilize the Ag nanoparticles onto the sidewalls of the HC-PCF core. The analyte–nanoparticle mixture was prepared by introducing a 10^{-6} M concentration of aqueous R6G into a solution containing: 25 nm Ag nanoparticles with a broad surface plasmon band peaked around 405 nm, and 10 mM of sodium chloride to induce nanoparticle aggregation in the mixture. The SERS spectra of R6G mixture were obtained and compared in two detection configurations after the mixture was filled into the Ag-nanoparticle-functionalized core of HC-PCF: (1) focus and collection light from the cladding-sealed end of the HC-PCF and (2) focus and collection light from the unsealed end of the of the HC-PCF. In both configurations, the SERS signals of R6G, obtained using a 633 nm laser, were stronger than that obtained from direct sampling of the R6G-Ag nanoparticle mixture. This indicated that

the Ag-functionalized HC-PCF further enhanced the SERS signals of R6G beyond that of which were obtained from the direct sampling of mixtures of R6G and Ag nanoparticles. This improved enhancement was the result of the increased light–analyte interaction, improved induction and collection efficiency of the pump laser and Raman scattering, respectively, and from potentially increasing hotspots with sandwiched Ag nanoparticle structures.

It is worth noting that the SERS signal obtained from the unsealed end of the HC-PCF was 10 times stronger than that from direct sampling while the SERS signal obtained from the cladding-sealed end was 100 times stronger. The enhancement difference was attributed to the "bowl" shape of the sealed end formed in the sealing process, which could mean that a larger volume of solution is found in the bowl in the sealed end, or that the Ag nanoparticles in the bowl could potentially improve the coupling of light into and out of the central core.

6. Summary

The integration of different optofluidic fibers with Raman spectroscopy to achieve enhancement in the retrieved Raman signal was reviewed. Recent progress in utilizing this novel enhancement technique for various applications in examining nanomaterials and biological samples was presented. Furthermore, recent efforts and applications in combining SERS with optofluidic fibers to achieve superior sensitivity in Raman spectroscopy were also reviewed.

Despite the advancements in this novel field of Raman spectroscopy, much work remains to be undertaken to achieve ultra-sensitive Raman analysis of many solutions of interest, particularly for nanomaterials in aqueous solutions and for biomolecules. Systemic optimization of the optical modes in the optofluidic devices for different nanomaterials and biological samples would benefit this sensitivity enhancement effort. This is particularly important in maximizing the retrieved Raman signal from a SERS-PCF integrated platform. In addition, more novel techniques of integrating SERS and other variations of Raman spectroscopy into optofluidic devices will be expected in the future to provide higher sensitivity.

Current optofluidic platforms provide little control over the fluidic flow of the analytes. Integration of the optofluidic fiber with advanced micro- and nano-fluidic elements would be essential in the future to realize the full potential of optofluidic devices for Raman spectroscopy. For example, solution mixing within the platform would be required for real time Raman analysis of many biological interactions. Removal of bubbles in micro- and nano-liters of samples would also be necessary to produce stable and reproducible results as well as assist in maximizing the retrieved Raman signal. Novel techniques to modify PCFs and TCTs for generating fluidic ports to the air core and holes with minimal effect on the optical guiding modes are still lacking.

While one-time use of the optofluidic fibers is ideal for biological studies, the ability to reuse the fibers would be of great importance for other applications involving nanoparticles or chemicals due to the high cost of the fibers. Development of a technique to clean optofluidic fibers from nanoparticles or other chemicals would be ideal in future studies.

Acknowledgments

This work was supported by Ontario Centers of Excellence and the Natural Sciences and Engineering Research Council of Canada.

References

[1] P. Baraldi, A. Tinti, Journal of Raman Spectroscopy 39 (2008) 963–965.
[2] P. Vandenabeele, F. Verpoort, L. Moens, Journal of Raman Spectroscopy 32 (2001) 263–269.
[3] P. Vandenabeele, J. Tate, L. Moens, Analytical and Bioanalytical chemistry 387 (2007) 813–819.
[4] P. Vandenabeele, T.L. Weis, E.R. Grant, L.J. Moens, Analytical and Bioanalytical chemistry 379 (2004) 137–142.
[5] M. Pérez-Alonso, K. Castro, J.M. Madariaga, Analytica Chimica Acta 571 (2006) 121–128.
[6] B.D. Patel, P.J. Mehta, Current Pharmaceutical Analysis 6 (2010) 131–141.
[7] T. Vankeirsbilck, A. Vercauteren, W. Baeyens, G. Van der Weken, F. Verpoort, G. Vergote, J.P. Remon, TrAC Trends in Analytical Chemistry 21 (2002) 869–877.
[8] P. Matoušek, M.D. Morris, Emerging Raman Applications and Techniques in Biomedical and Pharmaceutical Fields, Ebrary Inc., Springer, Heidelberg, 2010.
[9] E.V. Efremov, F. Ariese, C. Gooijer, Analytica Chimica Acta 606 (2008) 119–134.
[10] K. Nakamoto, Infrared and Raman Spectra of Inorganic and Coordination Compounds, Wiley, Hoboken, 2009.
[11] A.M. Kelley, Annual Review of Physical Chemistry 61 (2010) 41–61.
[12] K. Kneipp, H. Kneipp, I. Itzkan, R.R. Dasari, M.S. Feld, Journal of Physics: Condensed Matter 14 (2002) R597–R624.
[13] M. Li, J. Xu, M. Romero-Gonzalez, S.A. Banwart, W.E. Huang, Current Opinion in Biotechnology 23 (2012) 56–63.
[14] A. Downes, A. Elfick, Sensors 10 (2010) 1871–1889.
[15] A. Kumar, B.M. Boruah, X.-J. Liang1, Journal of Nanomaterials (2011)) .
[16] L.M. Almond, J. Hutchings, N. Shepherd, H. Barr, N. Stone, C. Kendall, Journal of Biophotonics 4 (2011) 685–695.
[17] M. Tanaka, R. Young, Journal of Materials Science 41 (2006) 963–991.
[18] J.M. Chalmers, H.G.M. Edwards, M.D. Hargreaves, Infrared and Raman Spectroscopy in Forensic Science, Wiley, Chichester, West Sussex, UK; Hoboken, 2012.
[19] V. Sikirzhytski, A. Sikirzhytskaya, I.K. Lednev, Applied Spectroscopy 65 (2011) 1223–1232.
[20] D.S. Moore, R. Jason Scharff, Analytical and Bioanalytical Chemistry 393 (2009) 1571–1578.
[21] A. Sarmiento, M. Maguregui, I. Martinez-Arkarazo, M. Angulo, K. Castro, M.A. Olazábal, L.A. Fernández, M.D. Rodríguez-Laso, A.M. Mujika, J. Gómez, J.M. Madariaga, Journal of Raman Spectroscopy 39 (2008) 1042–1049.
[22] U. Villanueva, J.C. Raposo, K. Castro, A.d. Diego, G. Arana, J.M. Madariaga, Journal of Raman Spectroscopy 39 (2008) 1195–1203.
[23] D. Larroumet, D. Greenfield, R. Akid, J. Yarwood, Journal of Raman Spectroscopy 39 (2008) 1740–1748.
[24] C.F. Bohren, D.R. Huffman, Absorption and Scattering of Light by Small Particles, Wiley, New York, 1983.
[25] H.A. Szymanski, Raman Spectroscopy: Theory and Practice, Plenum Press, New York, 1967.
[26] K. Kneipp, Y. Wang, H. Kneipp, L.T. Perelman, I. Itzkan, R.R. Dasari, M.S. Feld, Physical Review Letters 78 (1997) 1667–1670.
[27] E.C.L. Ru, P.G. Etchegoin, Annual Review of Physical Chemistry 63 (2012) 65–87.
[28] E.C.L. Ru, E. Blackie, M. Meyer, P.G. Etchegoin, Journal of Physical Chemistry C 111 (2007) 13794–13803.
[29] N.P. Pieczonka, R.F. Aroca, Chemical Society Reviews 37 (2008) 946–954.
[30] T. Chen, H. Wang, G. Chen, Y. Wang, Y. Feng, W.S. Teo, T. Wu, H. Chen, ACS Nano 4 (2010) 3087–3094.
[31] J. Guicheteau, L. Argue, A. Hyre, M. Jacobson, S.D. Christesen, Proceedings of SPIE 6218 (2006) 62180O.

[32] W. Xua, X. Linga, J. Xiaoa, M.S. Dresselhaus, J. Kongb, H. Xud, Z. Liua, J. Zhanga, Proceedings of the National Academy of Science USA 109 (2012) 9281–9286.
[33] A.G. Brolo, D.E. Irish, Journal of Electroanalytical Chemistry 414 (1996) 183–196.
[34] P.L. Stiles, J.A. Dieringer, N.C. Shah, R.P.V. Duyne, Annual Review of Analytical Chemistry 1 (2008) 601–626.
[35] G. Chen, Y. Wang, M. Yang, J. Xu, S.J. Goh, M. Pan, H. Chen, Journal of the American Chemical Society 132 (2010) 3644–3645.
[36] S.L. Kleinman, R.R. Frontiera, A.-I. Henry, J.A. Dieringer, R.P.V. Duyne, Phys. Chem. Chem. Phys. 15 (2012) 21–36.
[37] G.E. Walfaren, J. Stone, Spectroscopy 26 (1972) 585–589.
[38] H.B. Ross, W.M. McClain, Applied Spectroscopy 35 (1981) 439–442.
[39] G.E. Walfaren, Applied Spectroscopy 179 (1975) 179–185.
[40] W.J. Schmid, H.W. Schrotter, Journal of Raman Spectroscopy 10 (1981) 212–214.
[41] Z. Li, T. Chang, L.P.X. Sun, S. Gao, Chinese Physics Letters 10 (1993) 409–412.
[42] R. Altkorn, Applied Optics 36 (1997) 8992–8998.
[43] L. Song, S. Liu, V. Zhelyaskov, M.A. El-Sayed, Applied Spectroscopy 52 (1998) 1364–1367.
[44] D. Qi, A.J. Berger, Journal of Biomedical Optics 10 (2005) 031115.
[45] M. Holtz, P. Dasgupta, G. Zhang, Analytical Chemistry 71 (1999) 2934–2938.
[46] Y.-J. Tian, J. Zuo, L.-Y. Zhang, Z.-W. Li, S.-Q. Gao, G.-H. Lu, Applied Physics B 87 (2007) 727–730.
[47] R. Altkorn, I. Koev, M.J. Pelletier, Applied Spectroscopy 53 (1999) 1169–1176.
[48] M.A. Hossain, Y. Namihira, S.M.A. Razzak, Optical Review 19 (2012) 315–319.
[49] C.F. Kaminski, R.S. Watt, A.D. Elder, J.H. Frank, J. Hult, Applied Physics B 92 (2008) 367–378.
[50] A.V.V. Nampoothiri, A.M. Jones, C. Fourcade-Dutin, C. Mao, N. Dadashzadeh, B. Baumgart, Y.Y. Wang, M. Alharbi, T. Bradley, N. Campbell, F. Benabid, B.R. Washburn, K.L. Corwin, W. Rudolph, Optical Materials Express 2 (2012) 948–961.
[51] A. Tünnermann, S. Höfer, A. Liem1, J. Limpert, M. Reich, F. Röser, T. Schreiber, H. Zellmer, T. Peschel, V. Guyenot, Laser Physics 15 (2005) 107–117.
[52] K.P. Hansen, Journal of Optical and Fiber Communications Research 2 (2005) 226–254.
[53] F. Couny, F. Benabid, Journal of Optics A: Pure and Applied Optics 11 (2009) 103002.
[54] J. Irizar, J. Dinglasan, J.B. Goh, A. Khetani, H. Anis, D. Anderson, C. Goh, A.S. Helmy, IEEE Journal of Selected Topics in Quantum Electronics 14 (2008) 1214–1222.
[55] R.M. Abu-Ghazalah, J. Irizar, A.S. Helmy, R.B. Macgregor Jr, Biophysical Chemistry 147 (2010) 123–129.
[56] J.S.W. Mak, A.A. Farah, F. Chen, A.S. Helmy, ACS Nano 5 (2011) 3823–3830.
[57] F. Eftekhari, A. Lee, E. Kumacheva, A.S. Helmy, Optics Letters 37 (2012) 600–602.
[58] J.C. Knight, Conference on Optical Fiber Communication, OFC, San Jose, CA, 1996.
[59] P.S.J. Russell, Science 299 (2003) 358–362.
[60] J.C. Knight, T.A. Birks, P.S.J. Russell, D.M. Atkin, Optics Letters 21 (1996) 1547–1549.
[61] P.S.J. Russell, Journal of Lightwave Technology 24 (2006) 4729–4749.
[62] L. Dong, H.A. McKay, L. Fu, Optics Letters 33 (2008) 2440–2442.
[63] D. Pristinski, H. Du, Optics Letters 31 (2006) 3246–3248.
[64] Z. Xie, Y. Lu, H. Wei, J. Yan, P. Wang, H. Ming, Applied Physics B 95 (2009) 751–755.
[65] M.K.K. Oo, R.M. Yun Han, S. Sukhishvili, H. Du, Optics Letters 34 (2009) 968–970.
[66] M.K.K. Oo, Y. Han, J. Kanka, S. Sukhishvili, H. Du, Optics letters 35 (2010) 466–468.
[67] F. Benabid, Transactions of Royal Society A 364 (2006) 3439–3462.
[68] X. Yang, A.Y. Zhang, D.A. Wheeler, T.C. Bond, C. Gu, Y. Li, Analytical and Bioanalytical Chemistry 402 (2012) 687–691.
[69] M. Naji, Proceedings of SPIE 6865 (2008) 68650E.
[70] X. Yang, C. Shi, D. Wheeler, R. Newhouse, B. Chen, J.Z. Zhang, C. Gu, Journal of the Optical Society of America A 27 (2010) 977–984.
[71] T.A. Birks, J.C. Knight, P.S.J. Russell, Optics Letters 22 (1997) 961–963.
[72] J.D. Joannopoulos, R.D. Meade, J.N. Winn, Photonic Crystals : Molding the Flow of Light: Appendix C, Princeton University Press, Princeton, N.J., 1995.
[73] H. Xuan, W. Jin, J. Ju, H.L. Ho, M. Zhang, Y. Liao, Proceedings of SPIE 6619 (2007) 36–39.
[74] G. Antonopoulos, F. Benabid, T.A. Birks, D.M. Bird, J.C. Knight, P.S.J. Russell, Optics Express 14 (2006) 3000–3006.
[75] C.J.D. Matos, C.M.B. Cordeiro, E.M.d. Santos, J.S. Ong, A. Bozolan, C.H.B. Cruz, Optics Express 15 (2007) 11207–11212.

[76] W.M. Tolles, J.W. Nibler, J.R. McDonald, A.B. Harvey, Applied Spectroscopy 31 (1977) 253–271.
[77] F. Eftekhari, J. Irizar, L. Hulbert, A.S. Helmy, Journal of Applied Physics 109 (2011) 113104 113101.
[78] Y. Han, M.K.K. Oo, Y. Zhu, L. Xiao, M.S. Demohan, W. Jin, H. Du, Optical Engineering (2008) 040502.
[79] L. Huo, C. Lin, Y.K. Suen, S.K. Kong, in: Optical Fiber Communication and Optoelectronics Conference, Asia, 2007.
[80] S.A. Rutledge, A.A. Farah, J. Dinglasan, D.J. Anderson, A. Das, J. Goh, C. Goh, A.S. Helmy, Journal of Physical Chemistry C 113 (2009) 20208–20213.
[81] R.M. Abu-Ghazalah, S. Rutledge, L.W.Y. Lau, D.N. Dubins, R.B.M. J, A.S. Helmy, Biochemistry 51 (2012) 7357–7366.
[82] Y. Huang, Y. Xu, A. Yariv, Applied Physics Letters 85 (2004) 5182.
[83] C.M.B. Cordeiro, E.M.d. Santos, C.H.B. Cruz, C.J.d. Matos, D.S. Ferreiira, Optics Express 14 (2006) 8403.
[84] R. Altkorn, M.D. Malinsky, R.P. Van Duyne, I. Koev, Applied Spectroscopy 55 (2001) 373–381.
[85] A.L. Rogach, T. Franzl, T.A. Klar, J. Feldmann, N. Gaponik, V. Lesnyak, A. Shavel, A. Eychmüller, Y.P. Rakovich, J.F. Donegan, Journal of Physical Chemistry C 111 (2007) 14628–14637.
[86] H. Zhang, P. Sun, C. Liu, H. Gao, L. Xu, J. Fang, M. Wang, J. Liu, S. Xu, Luminescence 26 (2009) 86–92.
[87] J. Liu, Z. Shi, Y. Yu, R. Yang, S. Zuo, Journal of Colloid and Interface Science 342 (2010) 278–282 Epub 2009 Oct.
[88] C. Wang, H. Zhang, J. Zhang, M. Li, H. Sun, B. Yang, Journal of Physical Chemistry C 111 (2007) 2465–2469.
[89] M.S. Abd El-sadek, J. Ram Kumar, S. Moorthy Babu, Current Applied Physics 10 (2010) 317–322.
[90] K.-S. Cho, E.K. Lee, W.-J. Joo, E. Jang, T.-H. Kim, S.J. Lee, S.-J. Kwon, J.Y. Han, B.-K. Kim, B.L. Choi, Nature Photonics 3 (2009) 341–345.
[91] E.H. Sargent, Advanced Materials 20 (2008) 3958–3964.
[92] X. Qian, X.-H. Peng, D.O. Ansari, Q. Yin-Goen, G.Z. Chen, D.M. Shin, L. Yang, A.N. Young, M.D. Wang, S. Nie, Nature Biotechnology 26 (2008) 83–90.
[93] S. Kim, Y.T. Lim, E.G. Soltesz, A.M. De Grand, J. Lee, A. Nakayama, J.A. Parker, T. Mihaljevic, R.G. Laurence, D.M. Dor, Nature Biotechnology 22 (2004) 93–97.
[94] E. Yaghini, A.M. Seifalian, A.J. MacRobert, Nanomedicine 4 (2009) 353–363.
[95] O.R. Ochoa, E.J. Witkowski Iii, C. Colajacomo, J.H. Simmons, B.G. Potter Jr, Journal of Materials Science Letters 16 (1997) 613–616.
[96] V. Vinogradov, G. Karczewski, I. Kucherenko, N. Mel'nik, P. Fernandez, Physics of the Solid State 50 (2008) 164–167.
[97] P.M. Amirtharaj, F.H. Pollak, Applied physics Letters 45 (1984) 789–791.
[98] S.H. Shin, J. Bajaj, L.A. Moudy, D.T. Cheung, Applied Physics Letters 43 (1983) 68–70.
[99] G. Morell, A. Reynés-Figueroa, R.S. Katiyar, M.H. Farías, F.J. Espinoza-Beltran, O. Zelaya-Angel, F. Sánchez-Sinencio, Journal of Raman Spectroscopy 25 (1994) 203–207.
[100] B. Schreder, T. Schmidt, V. Ptatschek, U. Winkler, A. Materny, E. Umbach, M. Lerch, G. Muller, W. Kiefer, L. Spanhel, The Journal of Physical Chemistry B 104 (2000) 1677–1685.
[101] B. Schreder, T. Schmidt, V. Ptatschek, L. Spanhel, A. Materny, W. Kiefer, Journal of Crystal Growth 214-215 (2000) 782–786.
[102] A. Fischer, L. Anthony, A.D. Compaan, Applied Physics Letter 72 (1998) 2559–2561.
[103] R. Pal, J. Dutta, S. Chaudhuri, A.K. Pal, Journal of Physics D: Applied Physics 26 (1993) 704.
[104] J.E. Kim, Notes 29 (2008) 1247.
[105] H. Zhang, Z. Zhou, B. Yang, M. Gao, The Journal of Physical Chemistry B 107 (2002) 8–13.
[106] J.A. Kloepfer, S.E. Bradforth, J.L. Nadeau, The Journal of Physical Chemistry B 109 (2005) 9996–10003.
[107] J. Aldana, Y.A. Wang, X. Peng, Journal of the American Chemical Society 123 (2001) 8844–8850.
[108] K. Nakamoto, Infrared and Raman Spectra of Inorganic and Coordination Compounds: Part B, Wiley, Hoboken, 2009.
[109] G. Socrates, Infrared Characteristic Group Frequencies, Wiley, New York, 1980.
[110] M. Gao, S. Kirstein, H. Mohwald, A.L. Rogach, A. Kornowski, A. Eychmuller, H. Weller, The Journal of Physical Chemistry B 102 (1998) 8360–8363.
[111] H. Zhang, D. Wang, H. Möhwald, Angewandte Chemie International Edition 45 (2006) 748–751.
[112] P. Ghosh, G. Han, M. De, C.K. Kim, V.M. Rotello, Advanced Drug Delivery Reviews 60 (2008) 1307–1315.
[113] E.E. Connor, J. Mwamuka, A. Gole, C.J. Murphy, M.D. Wyatt, Small 1 (2005) 325–327.

[114] D. Pissuwan, T. Niidome, M.B. Cortie, Journal of Controlled Release 149 (2009) 65–71.
[115] X. Caoa, Y. Yeb, S. Liu, Analytical Biochemistry 417 (2011) 1–16.
[116] P.K. Jain, I.H. El-Sayed, M.A. El-Sayed, Nano Today 2 (2007) 18–29.
[117] E. Hutter, D. Maysinger, Microscopy Research and Technique 74 (2011) 592–604.
[118] M.A. Garcia, Journal of Physics D: Applied Physics 44 (2011) 283001.
[119] P. Mulvaney, Langmuir 12 (1996) 788–800.
[120] K. Kneipp, Y. Wang, R.R. Dasari, M.S. Feld, Applied Spectroscopy 49 (1995) 780–784.
[121] S. Nie, S.R. Emory, Science 275 (1997) 1102–1106.
[122] K. Kneipp, Y. Wang, H. Kneipp, L.T. Perelman, I. Itzkan, R.R. Dasari, M.S. Feld, Physical Review Letters 78 (1997) 1667–1670.
[123] K. Kneipp, H. Kneipp, R. Manoharan, I. Itzkan, R.R. Dasari, M.S. Feld, Bioimaging 6 (1998) 104–110.
[124] N.C.M. Tam, B.M.T. Scott, D. Voicu, B.C. Wilson, G. Zheng, Bioconjugate Chemistry 21 (2010) 2178–2182.
[125] C.H. Munro, W.E. Smith, M. Garner, J. Clarkson, P.C. White, Langmuir 11 (1995) 3712–3720.
[126] L. Jiang, J. Guan, L. Zhano, J. Li, W. Yang, Colloids and Surfaces A 346 (2009) 216–220.
[127] J. Schwan, S. Ulrich, V. Batori, H. Ehrhardt, S.R.P. Silva, Journal of Applied Physics 80 (1996) 440.
[128] S. Reich, C. Thomsen, Philosophical Transactions Series A, Mathematical, Physical, and Engineering Sciences 362 (2004) 2271–2288.
[129] A.C. Fagnano, G.F. Torreggiani, Biospectroscopy 2 (1996) 225–232.
[130] A. Torreggiani, Journal of Molecular Structure 480-481 (1999) 459–463.
[131] N. Uzunbajakava, A. Lenferink, Y. Kraan, E. Volokhina, G. Vrensen, J. Greve, C. Otto, Biophysics 84 (2003) 3968–3981.
[132] A. Barhoumi, D. Zhang, F. Tam, N.J. Halas, Journal of the American Chemical Society 130 (2008) 5523–5529.
[133] M. Gellert, M.N. Lipsett, D.R. Davies, Proceeding of National Academy of Science USA 48 (1962) 2013–2018.
[134] J.L. Huppert, S. Balasubramanian, Nucleic Acids Research 33 (2005) 2908–2916.
[135] A.K. Todd, M. Johnston, S. Neidle, Nucleic Acids research 33 (2005) 2901–2907.
[136] K. Poon, R.B. Macgregor Jr., Biophysical Chemistry 84 (2000) 205–216.
[137] E. Protozanova, R.B. Macgregor Jr., Biochemistry 35 (1996) 16638–16645.
[138] E. Protozanova, R.B. Macgregor Jr., Biophysical Chemistry 75 (1998) 249–257.
[139] K. Poon, R.B. Macgregor Jr., Biopolymers 45 (1998) 427–434.
[140] T. Miura, J.M. Benevides, G.J. Thomas Jr., Journal of Molecular Biology 248 (1995) 233–238.
[141] C. Krafft, J.M. Benevides, G.J. Thomas, Nucleic Acids Research 30 (2002) 3981–3991.
[142] T. Miura, G.J. Thomas Jr., Biochemistry 33 (1994) 7848–7856.
[143] K. Poon, R.B. Macgregor, Biophysical Chemistry 79 (1999) 11–23.
[144] T. Simonsson, Biological Chemistry 382 (2001) 621–628.
[145] E. Dias, J.L. Battiste, J.R. Williamson, Journal of the American Chemical Society 116 (1994) 4479–4480.
[146] Y. Wang, D.J. Patel, Structure 1 (1993) 263–282.
[147] G.N. Parkinson, M.P. Lee, S. Neidle, Nature 417 (2002) 876–880.
[148] K.N. Luu, A.T. Phan, V. Kuryavyi, L. Lacroix, D.J. Patel, Journal of the American Chemical Society 128 (2006) 9963–9970.
[149] A. Ambrus, D. Chen, J. Dai, T. Bialis, R.A. Jones, D. Yang, Nucleic Acids Research 34 (2006) 2723–2735.
[150] J. Dai, M. Carver, C. Punchihewa, R.A. Jones, D. Yang, Nucleic Acids Research 35 (2007) 4927–4940.
[151] A.T. Phan, K.N. Luu, D.J. Patel, Nucleic acids research 34 (2006) 5715–5719.
[152] Y. Xu, Y. Noguchi, H. Sugiyama, Bioorganic & Medicinal Chemistry 14 (2006) 5584–5591.
[153] D. Renciuk, I. Kejnovska, P. Skolakova, K. Bednarova, J. Motlova, M. Vorlickova, Nucleic Acids Research 37 (2009) 6625–6634.
[154] S. Kumar, A. Mohan, R. Guleria, Biomarkers 11 (2006) 385–405.
[155] S. Hanash, S. Pitteri, V. Faca, Nature 452 (2008) 571–579.
[156] D. Saerens, L. Huang, K. Bonroy, S. Muylderans, Sensors 8 (2008) 4669–4686.
[157] P.D.'. haeseleer, Nature Biotehnology 24 (2006) 959–961.
[158] K. Rikova, A. Guo, Q. Zeng, A. Possemato, H.H. Jian, J. Nardone, K. Lee, C. Reeves, Y. Li, Y. Hu, Z. Tan, M. Stokes, L. Sullivan, J. Mitchell, R. Wetzel, J. MacNeill, J.M. Ren, J. Yuan, C.E. Bakalarski, J. Villen, J.M. Kornhauser, B. Smith, D. Li, X. Zhou, S.P. Gygi, T.-L. Gu, R.D. Polakiewicz, J. Rush, M.J. Comb, Cell 131 (2007) 1190–1203.

[159] D. Salomon, R. Brandt, F. Ciardiello, N. Normanno, Critical Reviews in Oncology/Hematology 19 (1995) 183–232.
[160] J. Ludwig, J. Weinstein, Biology and Nature Reviews Cancer 5 (2005) 845–856.
[161] C.T. Nguyen, J.T. Niguyen, S. Rutledge, J. Zhang, C. Wang, G. Walker, Cancer Letters 292 (2010) 91–97.
[162] S. Keren, C. Zavaleta, Z. Cheng, A.D.L. Zerda, O. Gheysens, S.S. Gambhir, Proceedings of National Academy of Science 5 (2008) 5844–5849.
[163] X. Liu, M. Knauer, N.P. Ivleva, R. Niessner, C. Haisch, Analytical Chemistry 82 (2010) 441–446.
[164] U. Resch-Genger, M. Grabolle, S. Cavaliere-Jaricot, R. Nitschke, T. Nann, Nature Methods 5 (2008) 763–775.
[165] J.C.Y. Kah, K.W. Kho, C.G. Lee, International Journal of Nanomedicine 2 (2007) 785–798.
[166] S. Lee, S. Kim, J. Choo, S.Y. Shin, Y.H. Lee, H.Y. Choi, S. Ha, K. Kang, C.H. Oh, Analytical Chemistry 79 (2007) 916–922.
[167] X. Wang, X. Qian, J.J. Beitler, Cancer Research 71 (2011) 1526–1532.
[168] Z. Liu, S. Tabakman, S. Sherlock, X. Li, Z. Chen, K. Jiang, S. Fan, H. Dai, Nano Research 3 (2010) 222–223.
[169] M.Y. Sha, H. Xu, M.J. Natan, R. Cromer, Journal of the American Chemical Society 130 (2008) 17214–17215.
[170] J.L. Gong, Y. Liang, Y. Huang, J.W. Chen, J.H. Jiang, G.L. Shen, R.Q. Yu, Biosensors and Bioelectronics 22 (2007) 1501–1507.
[171] D.U. S, C.Y. Fu, K.S. Soh, B. Ramaswamy, A. Kumar, M. Olivo, Biosensors and Bioelectronics 33 (2012) 293–298.
[172] Y. Zhang, C. Shi, C. Gu, L. Seballos, J.Z. Zhang, Applied Physics Letters 90 (2007) 193504.
[173] P. Measor, L. Seballos, D. Yin, J.Z. Zhang, E.J. Lunt, A.R. Hawkins, H. Schmidt, Applied Physics Letters 90 (2007) 211107.
[174] W. Xu, S. Xu, Z. Lü, L. Chen, B. Zhao, Y. Ozaki, Applied Spectroscopy 58 (2004) 414–419.
[175] Z.G. Xie, Y.H. Lu, P. Wang, K.Q. Lin, J. Yan, H. Ming, Chinese Physics Letters 25 (2008) 4473–4475.
[176] T.S. Hauck, A.A. Ghazani, W.C.W. Chan, Small 4 (2008) 153–159.
[177] Y. Han, S. Tan, M.K.K. Oo, D. Pristinski, S. Sukhishvili, H. Du, Advanced Materials 22 (2010) 2647–2651.
[178] C. Shi, C. Lu, C. Gu, L. Tian, R. Newhouse, S. Chen, J.Z. Zhang, Applied Physics Letters 93 (2008) 153101.